

The authors would like to thank both reviewers for their insightful comments and for taking the time to report the many small typos which were unfortunately not caught by the author team. A point by point responds to the reviewer's comments can be found below.

Reviewer 1

One major concern is that in their calibration of the XSAPR2 data they state that there is no significant bias between the GPM reflectivities and the XSAPR2 reflectivities. However, in their own scatter plot, XSAPR2 looks to be about +2 or 3 dB hotter for reflectivities greater than about 25 dBZ, but it's hard to tell without applying statistical fits and tests. I am concerned that the agreement XSAPR2 and GPM at higher reflectivities (and hence higher rain rates) may not be as clear cut as is suggested in the paper.

Lines 316-319: I do not agree that there is no significant bias shown in this scatter plot. Figure 4d does look like there is a high bias in XSAPR2 when $Z > 25$ dBZ. Is it possible that the DPR data are contaminated by attenuation? Given the short wavelength I would think this would be a possibility. I think a more careful examination of this comparison is warranted

The concerns raised by the reviewer are valid and the authors agree that they should further discuss the caveats associated with such a cross-validation approach and slightly modify their conclusions. Please find below relevant excerpts from the revised manuscript. Note that we now do not refer to this procedure as a "calibration" procedure but rather to a "cross-validation methods". Moreover, it is worth nothing that most observations used in this comparison have reflectivity less than 25 dBZ. Data density is now displayed next to the revised c and d panels of Figure 4.

"Calibrating the XSAPR2 radar reflectivity measurements is more challenging since it does not perform profiling observations and as such it cannot be benchmarked against disdrometer and KAZR2 observations. Performing a physical subsystem calibration remains the best way to calibrate the XSAPR2 system. Prior to the ACE-ENA field campaign (06/2017) the ARM engineering team performed such a procedure which is expected to bring the calibration of the XSAPR2 system used in this study to within 1 dB. Here, in an effort to develop alternative calibration/cross-validation methods, we also compare the XSAPR2 radar observations to Global Precipitation Measurement (GPM) Ku-band frequency of the Dual-frequency Precipitation Radar (DPR) observation when the satellite track crosses within a 245 km radius of the XSAPR2 radar site. It is not expected that both sets of observations will perfectly match because of the different footprints, path lengths and surface returns of both radars but this comparison should at least provide some insight in the event that the difference between both sensors is larger than several dB. [...]

Beyond agreeing in their location, both radars (XSAPR2 and GPM DPR) are found to agree on the reflectivity intensity of these precipitation echoes. To confirm their agreement, we estimated Contour of Frequency by Altitude Diagram (CFAD) of the differences in radar reflectivities between the matched XSAPR2 and GPM DPR for all 1516 available observations (Fig. 4b). Above the height at which GPM DPR is known to suffer from surface echo contamination (i.e., 1.5 km), the comparison between XSAPR2 reflectivities and GPM DPR reflectivities shows no

noticeable difference (i.e., no bias). A scatter plot between the matched GPM DPR and XSAPR2 radar reflectivity for height above 1.5 km confirms the overall lack of bias beyond the expect 1 dB between the two radars at all reflectivity (Fig. 4d on which the orange line depicts the best fit to the data and the dashed line represent a perfect match between the datasets and the grey shading indicates the data density). As mentioned above, scatter is expected because of the differences in configuration of both radar systems. The cloud types present in the cases available could further enhance the impact of the radar system differences since the shallow clouds observed during the 3 overpasses are of similar or even smaller size compared to the GPM DPR footprint. Small clouds could lead to non-uniform beam filling issue and as such to the GPM DPR underestimating the reflectivity of these cloud system which could partially explain the seemingly “high” bias of the XSAPR2 in Fig. 4d. Knowing that the ARM engineering team had calibrated the XSAPR2 just before the observations used here were collected and because this comparison with the GPM DPR showed no bias larger than several dB we conclude that, for the observation period between 01/10/2018 to 04/01/2018, the XSAPR2 was reasonably well calibrated and does not require any radar reflectivity adjustments.”

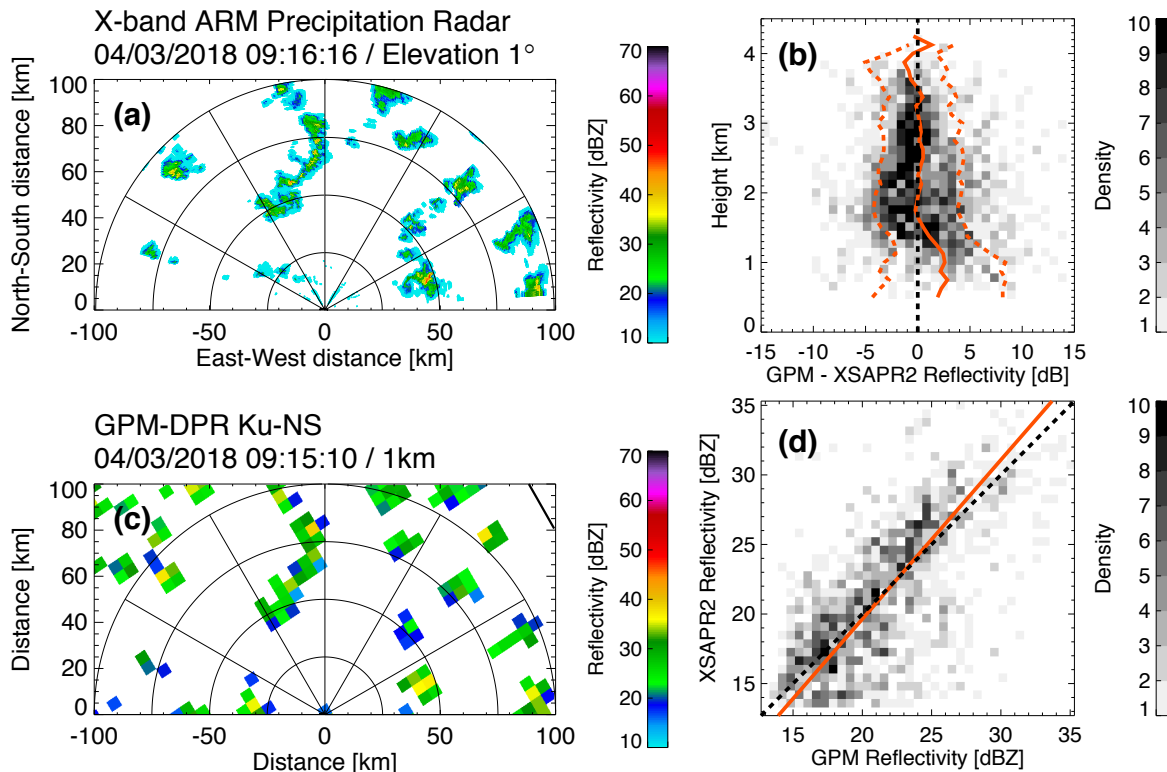


Figure 4. For the conditions that occurred on 04/03/2018 around 09:15 as observed by a) XSAPR2 radar reflectivity at 1° elevation and c) GPM-DPR Ku-band radar reflectivity at 1 km height. For the entire geometry-matching dataset with 1516 points used for the calibration b) Scatter, mean (orange) and standard deviation (dashed lines) of the difference between the GPM-DPR Ku-band and XSAPR2 radar reflectivity measurements as a function of height and d) scatterplot comparing the XSAPR2 and GPM-DPR Ku-band reflectivities measurements above the GPM surface echo height of 1.5 km; Also plotted is the 1-to-1 relationship (dashed line) and the best linear fit to the observations (solid orange line).

My other major concern is that the authors mention that “considerable differences in precipitation rate statistics estimated by XSAPR2 and KAZR2 challenge our ability to objectively estimate precipitation statistics over a domain.” I do not quite agree with this statement. The authors themselves have even established that XSAPR2 will provide better statistics simply due to the greater spatial coverage of XSAPR2. I think you can easily say that XSAPR2 is the better choice for deriving rainfall statistics simply due to its spatial coverage and reduced attenuation compared to KAZR2. So, I would like the authors to further clarify how these considerable differences between the two somehow complicate rainfall retrievals, because I honestly see a clear-cut choice here.

The authors agree with the reviewer that for the most part “Because of strong signal attenuation by gases and liquid at Ka-band, X-band radars are more suited for precipitation mapping especially over large domains.”. However, we want to acknowledge the one caveat: “When the character of precipitation varies rapidly with height for instance owing to an active evaporation process, zenith-pointing radars are more suited for precipitation characterization”.

The figures are also referred to out of order. For example, Figure 9 is referred to before Figure 6, which made it confusing for me to follow the figures. I would ask the authors in the next draft to place the figures in the order that they are referred to first in the paper. Also, there are incorrect references to Figure 7. I would urge the authors in the next draft to ensure that the Figures are also referred to correctly.

We apologize to the reviewer for the mix-up in figure references. Figures are now referred to in order and are properly referred to in the text.

Major comments:

Line 37: Are you missing a “these” here? Right now you are suggesting that observations in general cannot produce objective estimates of precipitation, which is definitely not the case for every single situation.

The reviewer is correct, the word “these” was added. Thank you.

Line 79: Is the lack of signal in KDP, ZDR simply a consequence of a narrower DSD that would be expected during the warm rain process?

The reviewer is correct, additional clarification is now given in the manuscript: “Beyond detecting, quantifying the spectrum from drizzle to rain from warm clouds is especially challenging since at small drizzle rates the droplets they contain are mostly spherical and as such do not generate the typical polarimetric signals required of common precipitation rate retrievals (e.g., Villarini and Krajewski, 2010; Gorgucci et al., 2000).”

Line 357-360: It actually looks like a lot of precipitation reaches the surface in Figure 5b, especially after 8 UTC. Could you please clarify in what conditions there is a more active evaporation process?

The reviews question is very interesting however we believe that documenting the conditions that lead to more or less drizzle evaporation is somewhat beyond the scope of this study which is focused on describing updated radar systems and on describing a precipitation retrieval technique.

Looking in literature we would say that our Figure 5a shows conditions consistent with Yang et al. (2018) study of single-layer marine stratocumulus clouds conducted in the Eastern North Atlantic where they report that drizzle is a common feature of marine stratocumulus cloud and that most of the drizzle drops evaporate in the subcloud layer before reaching the ground. In their study based on 42 days of stratocumulus cloud observations collected over a year, they found that 83% of the cloud profiles were drizzling with only 31% of them generating precipitation reaching the surface.

On the other hand, our Figure 5b shows a different scenario with a squall line probably associated with a cloud field deeper than a stratocumulus deck. The more intense rain produced by such cloud systems is most likely to not completely evaporate before reaching the surface; However, the gradient from green to blue seen in Figure 5b does support our statement that “the most intense precipitation rates are observed near cloud base height”.

Section 4.3: Why were two different tilts of KaSACR2 and XSAPR2 used here? These two radars could be showing areas scanned that are 0.5 km apart.

Although we agree with the reviewer that it would be optimum to compare KaSACR2 and XSAPR2 observations collected at the same 0.5° elevations tilt, our analysis of the prevalence of clutter in the XSAPR2 0.5° elevations tilt (Section 3.1) lead us to conclude that “Given this, XSAPR2 cross validation and precipitation rate maps will be estimated using observations collected at 1.0° elevation since it offers the best compromise between proximity to the surface and minimum sea-clutter contamination.” Unfortunately, KaSACR2 solely collected observations at 0.5° elevations tilt thus not allowing for a comparison between XSAPR2 and KaSACR2 1.0° elevations tilt.

We revised the text to reflect this reality:

“With the caveat that we are comparing rain rates retrieved at slightly different slanted elevations, comparing rain rates retrieved from the XSAPR2 observations (Fig. 8h) and from the KaSACR2 observations corrected for both gas and liquid attenuation (Fig. 8d) also highlights the fact that even after all correction are performed the KaSACR2 “realized” sensitivity does not allow it to detect some of the precipitation the more sensitive XSAPR2 can detect.”

Line 413: You mention that the two-way gas attenuation of XSAPR2 is negligible. However, attenuation from liquid at X-band can be significant, especially in the isolated deep convective cells. Have you applied any corrections for attenuation to the Z values in the development of your adaptive technique? Perhaps attenuation is not a major issue for the lighter precipitation events commonly observed at ENA, but I would foresee it being an issue in the isolated deep

convective cases. Therefore, I think it's necessary to factor in the potential effects of liquid attenuation in your analysis.

We completely agree with the reviewer that the decision of applying or not a liquid attenuation correction highly depends on the type of precipitation system. Text was added to the revised manuscript to reflect this comment.

“Note how the adaptive Z - R relationships were directly applied to clutter-filtered calibrated XSAPR2 radar reflectivity measurements since we estimate that, for the majority of the conditions occurring at the ENA observatory, both two-way gas attenuation and liquid attenuation at X-band are negligible; According to Rosenkranz (1998), at X-band frequency, gas attenuation generally amounts to 0.03 dB km^{-1} which is much smaller than even the radar calibration uncertainty. Similarly, Matrosov et al. (2005) discusses how, for rain rates of 2 mm hr^{-1} , liquid attenuation roughly amounts to 0.015 dB km^{-1} which over the depth of the shallow systems producing this type of precipitation cumulates to liquid attenuation less than 1 dB again within the radar calibration uncertainty. We do however acknowledge that, for deep convective systems, liquid attenuation correction would be granted, but since this type of precipitating system was not being frequently observed at the ENA observatory, we did not apply any liquid attenuation correction to the XSAPR2 measurements.”

Line 642-647: The considerable differences that we see are simply due to the very different samples that these instruments take. KAZR2 takes a soda straw view of the convection while XSAPR2 retrieves a full 3D volume. In addition, KAZR2 will be more heavily attenuated in heavy precipitation than XSAPR2. Therefore, these two p.d.f.s do not represent the same regions within the convection, and in general I would expect KAZR2 to not be as statistically representative of the observations simple due to the much lower sample volume you're factoring in. So, it's not a surprise that the statistics are so different for lower averaging intervals. Have you tried to compare the statistics where the two are scanning the same spot? For example, by comparing the statistics over a single gate of XSAPR2 that is directly over KAZR2?

Our intent is not to match the XSAPR2 and KAZR2 volume rather it is to confront this reality:

“The addition of the XSAPR2 at the ENA observatory offers new insights into precipitation variability and organization over a domain of 40-60 km radius around the size. However, the XSAPR2 data record is not as long as the KAZR data record which now spans 5 years at the ENA even totaling up to 7.5 years if we consider the Cloud, Aerosols, and Precipitation in the Marine Boundary Layer (CAP-MBL) campaign that took place at the site from April 2009 until January 2011 (Wood et al., 2005). Because of their longer data record, profiling radar observations have the potential to inform us about decadal precipitation variability both temporal and structural. However, with vertically pointing observations, it is near impossible to disentangle temporal evolution from horizontal structure. Classical approaches rely on Taylor hypothesis of frozen turbulence to convert elapsed time to horizontal dimension using the horizontal wind speed responsible for advecting cloud and precipitation overhead. While widely used, little research has been conducted to determine the validity and limitations of this assumption (see Oue et al. (2016) for a discussion on cloud fraction). In this section we seek to determine how long does one need to observe precipitation advected overhead to gather

statistical precipitation information equivalent to that of an 80 km wide domain.”

We attempt to address the difference in sensitivity of both system by “a minimum precipitation rate threshold of $10^{-2.8}$ mm hr⁻¹ is applied to both sensors reflecting the detectability of the XSAPR2 over the selected domain.”. Moreover, we limit the comparison domain to “40 km radius around the site”.

Following the reviewers comment, to improve at least the vertical collocation of both systems, we revised our approach as follows: “Although any height could be used, we perform this comparison at the specific height of 500 m; While KAZR2 precipitation retrievals can be directly extracted at 500 m, those from XSAPR2 must be extracted from gridded CAPPI fields which are constructed following the details provided in Section 6 using a collection of PPI scans.”

This new approached yield very similar conclusions:

“Focusing on features such as the width, the minimum, maximum and modes of the precipitation rate statistical distribution; Results indicate that neither 30 min nor 1h averaging of KAZR precipitation rate estimates can be used to replicate the precipitation rate statistics corresponding to those of domain averaged over 30 min (Fig. 10 left column). Averaging of 3 hrs of KAZR2 data improves its representativeness of domain average rain rate variabilities on scales of 1 to 3-hrs (2nd and 3rd rows/3rd column). Convergence between XSAPR2 and KAZR2 precipitation rate estimates is simingly best when considering the variability of domain-average precipitation rate over 12 h (correlation coefficient $R=0.25$) or longer timescales; 12-h average domain-average precipitation rate pdf from XSAPR2 and 12-h average precipitation rate pdf from KAZR are similar in both magnitude and mode location.”

“When it comes to capturing the general shape of the precipitation rate distribution, 12-hrs of zenith-pointing radar observations can be averaged to represent the 12-h variability of such a ~40 km radius half circle domain .”

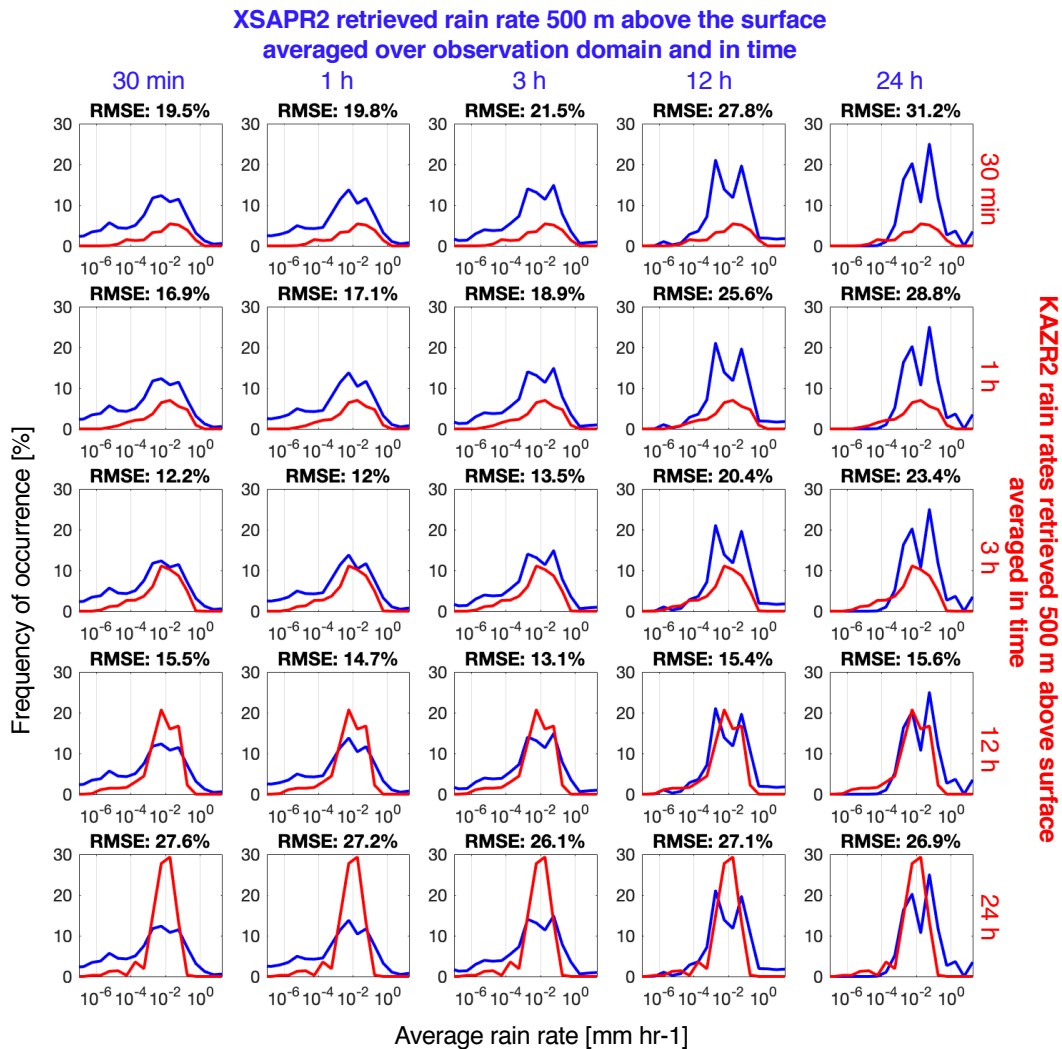


Figure 10. Probability density function of average (over different time windows) precipitation rate as estimated the XSAPR and by the KAZR2 (red) both at 500 m above the surface in $10^{0.5}$ mm hr⁻¹ bins; The XSAPR2 precipitation rates 500 m above the surface being from gridded CAPPI constructed using a collection of PPI scans and are limited to the domain between 2.5 and 40 km around the location of the KAZR2. Over each box is the correlation coefficient (R) between the XSAPR2 and the KAZR2 average precipitation rates.

Minor comments:

Abstract line 34: I would say the domain in terms of x by y km, not in km². This is generally more intuitive to the reader.

We agree with the reviewer; we now refer to the domain as a “40-km radius half circle”

Line 59: Run-on sentence here.

The sentence was broken down in two and slightly shortened: “Quantification, over a domain of

several kilometers, of marine drizzle cell precipitation rate and environmental conditions, could provide additional observational constraints for modeling studies. Unfortunately collecting such observations remain challenging over the ocean.”

Line 245: Extra “-” here.

We would like to thank the reviewer for reporting to typo. It was corrected.

Line 301: “XSAPR2.”

We would like to thank the reviewer for reporting to typo. It was corrected.

Line 316: Though should be “although.”

We would like to thank the reviewer for reporting to typo. It was corrected.

Figure 1: Your figures are not quite inside the boxes. Honestly, I would just remove the boxes around the figures.

Figure 1 was reproduced without the boxes.

The authors would like to thank both reviewers for their insightful comments and for taking the time to report the many small typos which were unfortunately not caught by the author team. A point by point responds to the reviewer's comments can be found below.

Reviewer 2

General comments:

1. I think the conclusion about the KaSACR2 precipitation rate would be more convincing if the paper shows some statistical analysis for a longer time period in addition to the theoretical sensitivity curve (Figure 9c) and one snapshot (Figure 7). Some further statistics would also help us better understand the bias of the KaSACR2 precipitation rate for marine boundary layer cloud regime.

We agree with the reviewer that a larger dataset would help further determine the potential of the KaSACR2 for precipitation characterization. However, here where both KaSACR2 and XSAPR2 observations were collected, we want to make the point that, simply from the standpoint of the radar specification, the XSAPR2 system is much more suited for precipitation studies:

“Now contrasting the two scanning radar XSAPR2 and KaSACR2. Although the Ka-band SACR2 experiences less sea-clutter than the X-band SAPR2, because of needs for cloud sampling, it only currently performs one PPI scan at 0.5° every 15 min which limits its temporal resolution. In addition, based on their technical specifications (Table 1), the XSAPR2 single pulse radar sensitivity is approximately 10 dB higher than that of the KaSACR2 (Fig. 9c blue and black line respectively). Finally, the Ka-band SACR2 also suffer from significantly more attenuation from atmospheric gases (Fig. 9c green line) and liquid water which even if corrected for still decrease it's “realized” sensitivity. For all these reasons, we conclude that the XSAPR2 is more suitable for characterizing light precipitation variability over large domains.”

We made sure to revise our final conclusions specifying that those apply to the XSAPR2 and not the KaSACR2:

“ 5) Shorter term domain precipitation rate variability can only be capture by scanning precipitation radars and especially those operating at weakly-attenuating frequencies and with high sensitivity such as the XSAPR2

6) Scanning sensors such as the XSAPR2 are also better suited to document sporadic and horizontal homogeneous precipitation including precipitation presenting mesoscale organization.”

2. It is not clear to me what time period, what weather conditions, and how many data samples are included in the analyses of Section 7.

We agree with the reviewer that it would be appropriate the restate the size of our dataset as it is relevant to the analysis of Section 7. We now specified in Section 7: “Over the 3-month period between 01/10/2018 and 04/01/2018, the domain representativeness of KAZR2 precipitation rate

estimates is evaluated using XSAPR2 observations collected over a domain of 40 km radius around the site.”.

3. This paper uses the XSAPR2 precipitation rate over a domain of 40 km radius around the site at 1° elevation and the KAZR2 precipitation rate at 200m above the surface to estimate the representativeness of zenith radar retrieved precipitation rate (Section 7). We know that the altitude of the XSAPR2 measurement increases with distance away from the radar (Figure 9a); and the XSAPR2 precipitation rate includes both horizontal and vertical variability (Figure 8), especially the vertical variability of the precipitation rate is pretty large in marine boundary layer cloud regime (e.g. Figure 5a). Therefore, this comparison is not just temporal vs. horizontal precipitation variability. I was not sure how to explain the convergence of these precipitation estimates at 12h and longer time scales shown in Figure 10. The paper demonstrates a gridded domain precipitation rate produce reconstructed from the XSAPR2 measurement in section 6 (Figure 9b). I wonder why this paper doesn't use the gridded data to estimate the representativeness of zenith radar retrieved precipitation rate. Also, I'd suggest the authors calculate the correlation coefficient between these two precipitation estimates, which provides more information about the relationship between these two precipitation estimates.

The reviewer's comment is a very good one. To this effect, we recomputed the pdfs using XSAPR2 500 m CAPPI precipitation rates and KAZR2 500 m precipitation rates and now report the correlation coefficient between the two. While the results differ somewhat, our conclusions change very little. Please find below our revisions of this section of the manuscript:

“Over the 3-month period between 01/10/2018 and 04/01/2018, the domain representativeness of KAZR2 precipitation rate estimates is evaluated using XSAPR2 observations collected over a domain of 40 km radius around the site. Although any height could be used, we perform this comparison at the specific height of 500 m; While KAZR2 precipitation retrievals can be directly extracted at 500 m, those from XSAPR2 must be extracted from gridded CAPPI fields which are constructed following the details provided in Section 6 using a collection of PPI scans. [...]

Focusing on features such as the width, the minimum, maximum and modes of the precipitation rate statistical distribution; Results indicate that neither 30 min nor 1h averaging of KAZR precipitation rate estimates can be used to replicate the precipitation rate statistics corresponding to those of domain averaged over 30 min (Fig. 10 left column). Averaging of 3 hrs of KAZR2 data improves its representativeness of domain average rain rate variabilities on scales of 1 to 3-hrs (2nd and 3rd rows/3rd column). Convergence between XSAPR2 and KAZR2 precipitation rate estimates is seemingly best when considering the variability of domain-average precipitation rate over 12 h (correlation coefficient $R=0.25$) or longer timescales; 12-h average domain-average precipitation rate pdf from XSAPR2 and 12-h average precipitation rate pdf from KAZR are similar in both magnitude and mode location.

Although these results are estimated with few observational cases (3-month period), they clearly suggest that XSAPR2 observations are necessary to characterize short-term (< 1 h) domain-average precipitation rate characteristics. They also suggest that longer-term (12 h) domain-average precipitation rate characteristics can be estimated by averaging either XSAPR2 or KAZR2 observations using time-windows of similar lengths.”

“When it comes to capturing the general shape of the precipitation rate distribution, 12-hrs of zenith-pointing radar observations can be averaged to represent the 12-h variability of such a ~40 km radius half circle domain .”

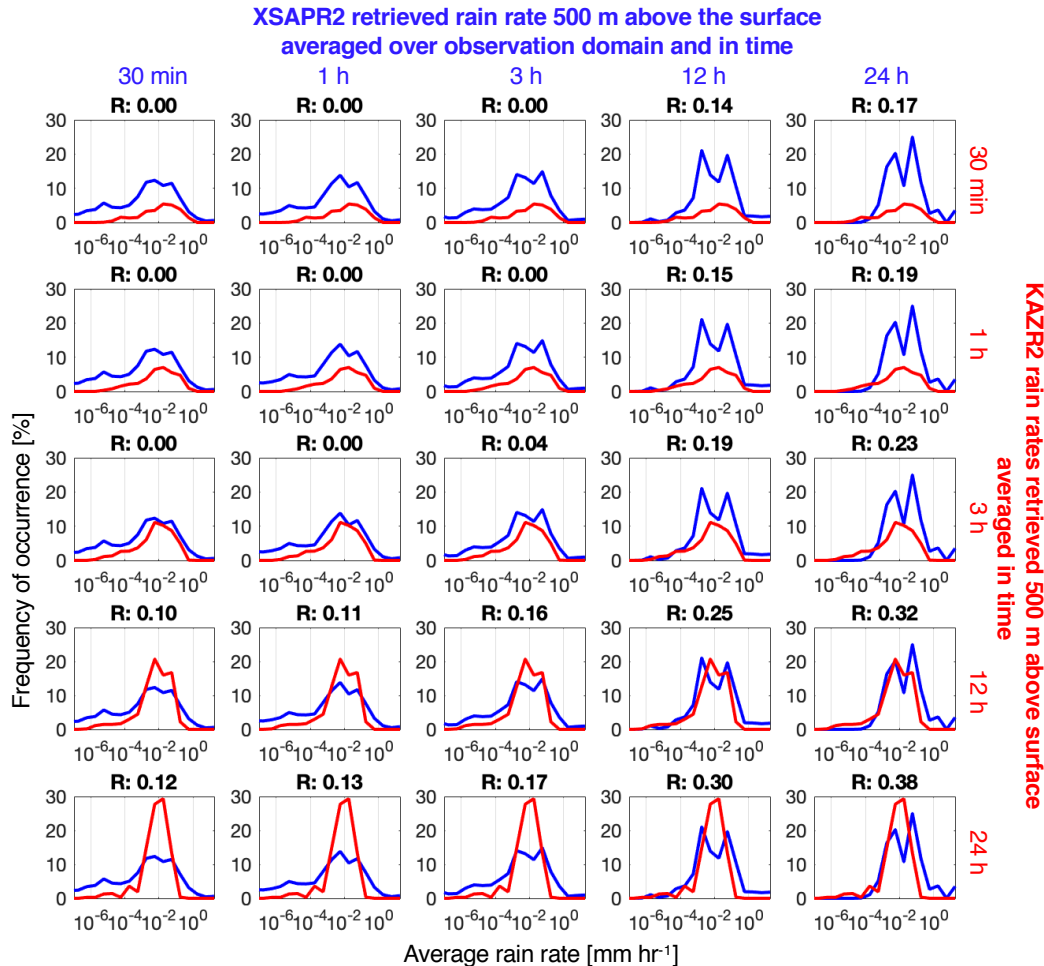


Figure 10. Probability density function of average (over different time windows) precipitation rate as estimated the XSAPR and by the KAZR2 (red) both at 500 m above the surface in $10^{0.5}$ mm hr⁻¹ bins; The XSAPR2 precipitation rates 500 m above the surface being from gridded CAPPI constructed using a collection of PPI scans and are limited to the domain between 2.5 and 40 km around the location of the KAZR2. Over each box is the correlation coefficient (R) between the XSAPR2 and the KAZR2 average precipitation rates.

Specific comments:

1. I've noticed some typos scattered throughout the manuscript, so I'd recommend a close readthrough before resubmission.

We would like to apologize to the reviewer for our oversights. We were more careful as we revised the manuscript.

2. Line 59: This sentence (and a few other sentences) should be separated into two sentences.

The sentence was broken down in two and slightly shortened: “Quantification, over a domain of several kilometers, of marine drizzle cell precipitation rate and environmental conditions, could provide additional observational constraints for modeling studies. Unfortunately collecting such observations remain challenging over the ocean.”

3. Line 95: “retrieved” → “retrieve”

We would like to thank the reviewer for reporting to typo. It was corrected.

4. Line 101: “The ENA” → “ENA” or “The ENA observatory”

Changed for “The Eastern North Atlantic region”.

5. Line 324-325: This sentence seems unnecessary to me.

The sentence was removed.

6. Line 353: “In additional to” → “In addition to”

We would like to thank the reviewer for reporting to typo. It was corrected.

7. Line 424: The referred figure jumps from Fig. 6 to Fig. 9.

We apologize to the reviewer for the mix-up in figure references. Figures are now referred to in order and are properly referred to in the text.

8. Line 433-437: The Figure number is wrong (I guess it should be Figure 7).

We apologize to the reviewer for the mix-up in figure references. Figures are now referred to in order and are properly referred to in the text.

9. Line 620: “were showed to” → “were shown to”

We would like to thank the reviewer for reporting to typo. It was corrected.

10. Figure 4. The red lines in (b) have not been defined in the caption.

We apologize for the oversight. The red lines in b depict the mean and standard deviation. The figure caption was revised accordingly.

11. Figure 5. Can you add the main wind direction on (c) and (d)? It may help us better understand the results from the zenith radar and the scanning radar.

The general wind direction was added using arrows in panels c-d.

12. Figure 6(c). I'm not sure why the solid line (median) is away from the higher frequency of occurrence range (the orange color $a = 1.5e2$) between $z = 0.8\text{km}$ and $z = 1.2\text{ km}$.

We verified and the position of the solid white line reflect the mean of the measurements at each height, the median is to the left of the region with the highest density of points since the distribution is skewed.

13. Figure 7. "The upper panel" → "The bottom panel"

We would like to thank the reviewer for reporting to typo. It was corrected.

14. Figure 10. The x axis of the subpanels and the caption "precipitation rate estimated in 0.5 mm hr-1 bins between -8 and 0.5 mm hr-1": I don't understand why there are negative precipitation rates in the results.

Rain rate are reported in logarithmic scale and the caption should read "precipitation rate estimated in $10^{0.5}$ mm hr⁻¹ bins between 10^{-8} and $10^{0.5}$ mm hr⁻¹." We would like to apologize to the reviewer for the confusion.

15. The paper argues that "forward-simulators should be used to guide high temporal-resolution model evaluation studies" without providing any information about forward-simulators. I would suggest the authors to briefly describe what forward-simulators are and cite a few relevant references.

We agree with the reviewer that additional information is granted, we added to following material to the revised manuscript:

"Factors such as instrument sensitivity, sampling resolution, sampling height and domain size should always be considered when comparing model output to observations. One way to consider these factors could be to convert model output rain rates to observable rain rate through the use of forward simulators which can use drop size and atmospheric conditions information to reproduce the attenuation affecting radar signals. Several forward-simulator further take into consideration the dependency of radar sensitivity with range which dictates the minimum detectable rain rate at various distance within a domain (e.g., Tatarevic et al., 2015; Lamer et al., 2018)."

1 Characterization of Shallow Oceanic Precipitation using Profiling
2 and Scanning Radar Observations at the Eastern North Atlantic ARM
3 Observatory

4 Katia Lamer¹, Bernat Puigdomènech Treserras², Zeen Zhu³, Bradley Isom⁴, Nitin Bharadwaj⁴, and
5 Pavlos Kollias^{3,5}

6
7
8 ¹. Department of Earth and Atmospheric Science, The City College of New York

9 ². Department of Atmospheric and Oceanic Sciences, McGill University

10 ³. School of Marine and Atmospheric Sciences, Stony Brook University

11 ⁴. Atmospheric Measurement and Data Sciences, Pacific Northwest National Laboratory

12 ⁵. Department of Environmental and Climate Sciences, Brookhaven National Laboratory

13

14 Correspondence: Katia Lamer, klamer@ccny.cuny.edu

15

16 **Abstract**

17

18 Shallow oceanic precipitation variability is documented using 2nd generation radars located
19 at the Atmospheric Radiation Measurement (ARM) Eastern North Atlantic observatory: The Ka-
20 band ARM zenith radar (KAZR2), the Ka-band scanning ARM cloud radar (KaSACR2) and the
21 X-band scanning ARM precipitation radar (XSAPR2). First, the radars and measurement post-
22 processing techniques, including sea clutter removal and calibration against collocated
23 disdrometer and Global Precipitation Mission (GPM) observations are described. Then, we present
24 how a combination of profiling radar and lidar observations can be used to estimate adaptive (in
25 both time and height) parameters that relate radar reflectivity (Z) to precipitation rate (R) in the
26 form $Z = \alpha R^\beta$ which we use to estimate precipitation rate over the domain observed by XSAPR2.
27 Furthermore, Constant Altitude Plan Position Indicator (CAPPI) gridded XSAPR2 precipitation
28 rate maps are also constructed.

29

30 Hourly precipitation rate statistics estimated from the three radars differ; that is because KAZR2
31 is more sensitive to shallow virga and because XSAPR2 suffers from less attenuation than
32 KaSACR2 and as such is best suited to characterize intermittent and mesoscale-organized
33 precipitation. Further analysis reveals that precipitation rate statistics obtained by averaging 12h
34 of KAZR2 observations can be used to approximate that of a 40-km radius domain averaged over
35 similar time periods. However, it was determined that KAZR2 is unsuitable to characterize domain
36 average precipitation rate over shorter periods. But even more fundamentally, these results suggest
37 that these observations cannot produce objective domain precipitation estimate and that the
38 simultaneous use of forward-simulators is desirable to guide model evaluation studies.

39

40

41

42

43

44

45

Deleted: the

Deleted: of 2,500 km²

Deleted: should be used

Deleted: high temporal-resolution

50 **1.0 Introduction**

51

52

53

54

55

56

57

58

59

60

61

62

63

64

65

66

67

68

69

70

71

72

73

74

75

76

77

78

79

80

81

82

83

84

85

86

87

88

89

90

91

92

93

94

95

Characterizing shallow oceanic precipitation is all-important to improving our understanding of shallow cloud systems since precipitation is related to a number of cloud process all of which may affect cloud properties. For example, precipitation leads to a reduction in the droplet number via the collision-coalescence process and of the liquid water path through sedimentation. Furthermore, a number of modeling studies have suggested that drizzle organization, intensity and subcloud layer evaporation could play a role in organizing stratocumulus cloud decks on the mesoscale (Zhou et al., 2017; Savic-Jovicic and Stevens, 2008; Wang and Feingold, 2009; Yamaguchi and Feingold, 2015; Zhou et al., 2018). Ultimately, these controls may alter low cloud radiative properties and climate (Wood, 2012). Quantification, over a domain of several kilometers, of marine drizzle cell precipitation rate and environmental conditions, could provide additional observational constrains for modeling studies. Unfortunately collecting such observations remain challenging over the ocean.

Although satellite-based microwave sensors can infer the spatial distribution of liquid water path (Wood and Hartmann, 2006; Miller and Yuter, 2013) and precipitation rate (Ellis et al., 2009; Adler et al., 2009; Rapp et al., 2013) they have poor horizontal resolution and suffer from surface inference causing them to under sample the cloud field variability and to underreport boundary-layer cloud and precipitation occurrence (Schumacher and Houze Jr, 2000; Rapp et al., 2013). In contrast, airborne (Stevens et al., 2005; Wood et al., 2011; Moyer and Young, 1994; Vali et al., 1998; Paluch and Lenschow, 1991; Sharon et al., 2006) and ship-based (Yuter et al., 2000; Comstock et al., 2005; Feingold et al., 2010) sensors can resolve the spatial/temporal variability of the cloud and precipitation field, but field campaigns deploying such sensors are often expensive to conduct and limited in temporal duration (Stevens et al., 2003; Bretherton et al., 2004; Rauber et al., 2007). Island-based observatories such as the U.S. Department of Energy (DOE) Atmospheric Radiation Measurement (ARM) Eastern North Atlantic observatory (ENA, Mather et al., 2016; Kollias et al., 2016) and the Barbados Cloud Observatory (BCO, Lamer et al., 2015; Stevens et al., 2016) operating profiling and scanning remote sensors can provide long-term statistics of marine light precipitation.

Beyond detecting, quantifying the spectrum from drizzle to rain from warm clouds is especially challenging since at small drizzle rates the droplets they contain are mostly spherical and as such do not generate the typical polarimetric signals required of common precipitation rate retrievals (e.g., Villarini and Krajewski, 2010; Gorgucci et al., 2000). As an alternative to polarimetric signatures, a combination of sensors is typically required to retrieve precipitation rate (R); Combinations of radar reflectivity (Z) and in-situ measurements have led to the development of Z - R relationships (Wood, 2005; Comstock et al., 2004; VanZanten et al., 2005; Vali et al., 1998) however, these tend not to be universally applicable since they are based on assumptions about the drizzle particle size distribution which may vary with factors such as aerosol loading and liquid water path. Moreover, relying on surface disdrometer measurements to characterize warm precipitation may be especially unsuitable at the ENA where i) a large fraction of the precipitation does not reach the surface (Yang et al., 2018), ii) precipitation reaching the ground typically does so with an intensity below the detection limit of most optical-based disdrometers ($\sim 10^{-2}$ mm hr^{-1}) and iii) evaporation is an active process such that water drop size distribution information retrieved at one height may not be appropriate to represent the entire atmospheric column.

Deleted: along with sub cloud layer evaporation rate, thermodynamic properties and dynamics

Deleted: u

Deleted: ,

Deleted: to collect

Deleted:

Deleted: precipitation rate

103 Alternatively, a method combining radar reflectivity and lidar backscatter measurements has been
104 proposed to retrieve R with fewer assumptions about the drizzle particle size distribution (Intrieri
105 et al., 1993; O'Connor et al., 2005); Because of the current rarity of scanning lidar observations,
106 this technique has only been used to retrieve R in the column and cannot be used to address the
107 concerns present in recent studies suggesting that scanning systems are essential to map domain
108 properties (Oue et al., 2016).

Deleted: out

Deleted: d

109
110 Here we propose to exploit the availability of collocated vertically-pointing radar and lidar as well
111 as scanning radar systems to characterize marine precipitation rate variability over a domain of 40-
112 60 km around the ENA observatory. The Eastern North Atlantic region, with its abundance of
113 marine boundary layer precipitating clouds, is an ideal location for such study (Rémillard and
114 Tselioudis, 2015; Wood, 2012). Observations from the Ka-band ARM Zenith Radar (KAZR2) and
115 zenith-pointing ceilometer lidar are combined to estimate adaptive (both in time and height) Z - R
116 relationships which we then use to estimate precipitation rate across the domain observed by the
117 X-band Scanning ARM Precipitation Radar (XSAPR2). Domain-average and time-average
118 precipitation rate estimates obtained from zenith-pointing and scanning observations are compared
119 to document the complementarity and applicability of each sensor in documenting precipitation
120 rate from warm boundary layer clouds.

Deleted: ENA

121 122 2.0 Eastern North Atlantic Observatory

123
124 In October 2013, the ARM program established a permanent observatory in the Eastern North
125 Atlantic on the island of Graciosa (~60 km² area; 39.1°N, 28.0°W). The site, located within the
126 Azores archipelago, straddles the boundary between the subtropics and the midlatitudes and as
127 such is subject to a wide range of different meteorological conditions including periods of
128 relatively undisturbed trade-wind flow, midlatitude cyclonic systems and associated fronts, and
129 periods of extensive low-level cloudiness (Rémillard and Tselioudis, 2015). The observatory hosts
130 an extensive instrument suite including three second generation radar systems: The Ka-band ARM
131 Zenith Radar (KAZR2), the dual-frequency Ka-and W-band Scanning ARM Cloud Radar
132 (SACR2) and the X-band Scanning ARM Precipitation Radar (XSAPR2) which's specifications
133 are listed in Table 1. A short description of the radar systems is provided here with emphasis on
134 changes in configuration from the first to the second generation.

Deleted: the

135 136 2.1 KAZR2

137
138 KAZR2 operates at 34.8 GHz ($\lambda = 8.6$ mm) and is an upgraded version of the KAZR that
139 replaced the ARM MilliMeter Cloud Radar (MMCR, Kollias et al., 2016). KAZR2 uses an
140 Extended Interaction Klystron (EIK) amplifier with a 2.2 kW peak power and 5 % duty cycle. Its
141 dual receiver configuration allows for the simultaneous transmission of two pulses: i) A long (4
142 μ s) pulse with frequency modulation (pulse compression) for higher sensitivity (~44 dBZ at 1 km
143 not considering signal integration gain) at ranges from 737 m from the radar to 18 km and ii) A
144 short pulse (200 ns) with a sensitivity of (~32.5 dBZ at 1 km not considering signal integration
145 gain) at ranges from 72 m to 18 km from the radar. KAZR2 has a narrow (0.3°) 3-dB antenna
146 bandwidth and is nominally operated with a range resolution of 30 m, a temporal resolution of 2
147 sec and is set to record the full radar Doppler spectrum with 256 or 512 FFT points. KAZR2
148 transmits a horizontal pulse and receives both horizontal and vertical polarization such that the

Deleted: a

Deleted: a

155 only polarimetric information it can measure is linear depolarization ratio.

156

157 2.2 KaSACR2

158

159 KaSACR2 is a fully polarimetric radar that operates at 35.3 GHz ($\lambda = 8.5$ mm) and is an
160 upgraded version of the single polarization KaSACR described in Kollias et al., (2014a,b). The
161 KaSACR2 also uses an EIK amplifier with a 2.2 kW peak power, has a 5 % duty cycle and a 3-dB
162 antenna beamwidth of 0.3°. Currently, it is operated with a short pulse, although it could be
163 operated with a longer pulse with pulse compression for increased sensitivity. Owing to its narrow
164 beam width KaSACR2 must scan rather slowly ($3\text{-}6^\circ \text{ s}^{-1}$) to collect observation with a sensitivity
165 of ~ 15 dBZ at 20 km (not considering signal integration gain). The KaSACR2 conducts a cloud
166 sampling strategy that includes different modes (Kollias et al., 2014a,b). Here, because of our
167 interest to map precipitation structure and rate over a large horizontal domain, we only use
168 observations collected in Plan Position Indicator (PPI) configuration only available at 0.5°
169 elevation angle over a 160° wide azimuth sector. The KaSACR2 conducts a PPI scan every 15 min
170 and takes 2 min to collect each PPI. The KaSACR2 employs frequency hopping and staggered
171 pulse repetition time techniques to mitigate artifacts due to second trip echoes and velocity
172 aliasing; This however comes at the expense of preventing the collection of the full Doppler
173 spectrum.

174

175 2.3 XSAPR2

176

177 XSAPR2 operates at 9.5 GHz ($\lambda = 3.2$ cm); It is an upgraded version of the XSAPR as it
178 operates with an improved digital receiver and a larger antenna (5 m) which results to an
179 exceptionally narrow 3-dB antenna beamwidth of 0.45°. The requirement for the XSAPR2 to have
180 a narrow antenna beamwidth emerged from two main needs: i) To reduce the impact of sea-clutter
181 at low-elevations and ii) maintain high angular resolution over a 60 km radius in order to resolve
182 small scale oceanic precipitating clouds. XSAPR2 uses a high-power Magnetron with a 300kW
183 peak power and a maximum duty cycle of 0.1 %. Under nominal operational conditions, the
184 XSAPR2 transmits a 60 m long pulse and scans at a relatively slow rate (6° s^{-1}) to collect
185 observations with a sensitivity of ~ 21 dBZ at 20km (not considering integration gain). The
186 XSAPR2 volume coverage pattern (VCP) scan strategy consists of a series of PPI scans every 0.5°
187 elevation between the angles of 0° and 5°. Because of considerable beam blockage in the southerly
188 direction a 160° azimuth sector coverage is achieved. The VCP scan (i.e. the entire set of PPI
189 scans) is completed within 5 min and subsequently repeated. Horizontal and vertical polarization
190 are possible for both transmit and receive states, meaning XSAPR2 collects a full suite of
191 polarimetric variables while in scanning mode.

192

193 3.0 Radar Observations Post-Processing

194

195 Radar observations require considerable post-processing for the removal of non-
196 meteorological targets before they can be scientifically interpreted or used to retrieve geophysical
197 quantities such as precipitation rate. Radar data post-processing is described in section 3.1 and
198 cross-comparison between different systems for calibration is described in section 3.2. Note that
199 the KAZR2 data used for analysis are from “enakazrgeC1.a1” files, KaSACR2 data are from

Deleted:

Deleted: at

Deleted: a

Deleted: t

204 “enakasacrppivhC1.a1” files and the XSAPR2 from the “enaxsaprsecD1.00 files”. All data files
205 were obtained from the ARM archive (<https://www.archive.arm.gov/discovery/>).
206

207 3.1 Removal of Non-Meteorological Targets

208 First, signal processing artifacts (e.g. second trip echoes) and echoes of non-meteorological
209 origin (e.g., biological echoes, sea-clutter, and ground-clutter) are identified and removed.
210

211
212 The KaSACR2 system operates in fully polarimetric mode and uses staggered pulse repetition time
213 and frequency hopping to automatically remove second trip echoes, perform velocity dealiasing
214 and increase the number of independent samples (Pazmany et al., 2013). The XSAPR2 systems
215 operates using a magnetron system which is coherent on receive (i.e., transmitted pulse phase is
216 random). For the XSAPR2, the removal of second trip echoes is done using Normalized Coherent
217 Power (NCP) which is the coherency of the received pulse with respect to the last transmitted
218 pulse. For atmospheric echoes within maximum unambiguous range, NCP is high since the radar
219 receiver is phase-locked to the phase of the last transmitted pulse. Outside of the maximum
220 unambiguous range, NCP is low since the radar receiver has already phase-locked on the phase of
221 another transmitted pulse. Here, an NCP threshold of 0.3 is used to identify echoes originating
222 from outside the maximum unambiguous range (i.e. second trip echoes).
223

224 Biological targets such as insect and birds often contaminate radar observations especially over
225 land (e.g., Luke et al., 2008). Their occurrence varies with atmospheric condition, time of the year,
226 and time of the day (Alku et al., 2015). KAZR2 observations at the ENA seem minimally impacted
227 by biological echoes. Furthermore, the fact that the bulk of the KaSACR2 and XSAPR2
228 observations are collected over open ocean and that Graciosa is a small island suggests that
229 biological targets should not be a concern at this particular location.
230

231 On the other hand, low elevation angle observations are susceptible to sea-clutter contamination.
232 Research on radar sea-clutter characterization and remediation has been ongoing for over 20 years
233 (e.g., Horst et al., 1978; Gregers-Hansen and Mital, 2009; Nathanson et al., 1991); Observational
234 and modeling studies suggest that factors such as oceanic wave properties (related to local wind
235 speed and direction), swell and air density streams can affect sea-clutter occurrence. Radar
236 characteristics such as wavelength, wave polarization, beam width and grazing angle are also
237 known to affect sea-clutter characteristics, amounts and our ability to isolate atmospheric returns
238 from sea-clutter. Here, observations collected over a range of wind conditions during nearly 100
239 hours of clear sky conditions are used to examine how sea-clutter characteristics vary with radar
240 wavelength, beam width and beam elevation angle.
241

242 First, the distribution of sea-clutter reflectivities as measured by the XSAPR2 and KaSACR2 at
243 elevation 0.5° are compared to document the antenna beam width effect (Fig. 1d). The KaSACR2
244 (0.3° 3-dB antenna beam width) sea-clutter reflectivity distribution is narrower with a peak at -21
245 dBZ and a majority of echoes below -15 dBZ (Fig. 1d black line) while the XSAPR2 (0.45° 3-dB
246 antenna beam width) sea-clutter reflectivity distribution is wider, peaks at -18 dBZ and covers a
247 range from -40 dBZ to +10 dBZ (Fig. 1d red line). This can be explained by the XSAPR2 wider
248 antenna beam width which results in a larger fraction of the radiated energy to hit ocean waves,
249 causing higher ocean clutter return power. Similar to beam width, elevation angle affects how

250 much sea is in the radar field of view and the spatial extent of observed sea-clutter. Figure 1d,
251 shows that, at 1.0° elevation, XSAPR2 sea-clutter reflectivity peaks at a lower reflectivity of -25
252 dBZ (blue line) and Fig. 1b₃ shows that in this configuration it frequently (> 25 % of the time)
253 detects clutter only over a domain of 10 km radius around the site which is much less than it detects
254 when collecting observations at 0.5° elevation (significant clutter in a 20 km radius around the
255 site Fig. 1a₃).
256

257 Now that we have characterized sea-clutter intensity and frequency of occurrence using clear sky
258 observations, we next evaluate its impact on the detection of meteorological targets using
259 observations containing mixture of hydrometeor and sea-clutter. To isolate hydrometeors from
260 clutter, we exploit the correlation coefficient ρ_{HV} which we know is affected by the relative
261 occurrence of signal to clutter; ρ_{HV} is typically close to 1 for liquid-phase hydrometeors and lower
262 for non-meteorological targets. Looking at KaSACR2 reflectivity and ρ_{HV} confirms that at Ka-
263 band wavelength the signal to clutter ratio is high and hydrometeors contributions dominate both
264 radar reflectivity and correlation coefficient measurements (Fig. 1c₁ and 1c₂, respectively). The
265 enhanced KaSACR2 signal-to-clutter ratio is attributed to two effects: i) its narrow beamwidth
266 which causes a smaller fraction of the transmitter energy to hit the sea surface and ii) its shorter
267 wavelength which creates a larger distinction between hydrometeor scattering - which follow
268 Rayleigh scattering $\sim 1/\lambda^4$ - and sea-clutter scattering - which follow $\sim 1/\lambda$. Using KaSACR2
269 observations has a guide to locate cloud and precipitation location (Fig 1c₁), it is apparent that it
270 is not possible to distinguish atmospheric signals from sea-clutter in XSAPR2 radar reflectivity
271 observation collected at 0.5° (Fig. 1a₁).
272

273 Several techniques that use both time-domain and frequency domain filtering methods have been
274 proposed to discriminate between sea-clutter and meteorological targets in precipitation radar
275 observations (e.g., Torres and Zrníc, 1999; Siggia and Passarelli, 2004; Nguyen et al., 2008; Alku
276 et al., 2015). Ryzhkov et al. (2002) present an echo classification technique based on fuzzy logic
277 and a multiparameter dataset including radar reflectivity, mean Doppler velocity, spectrum width,
278 differential reflectivity, differential phase, linear depolarization ratio, and cross-correlation (ρ_{HV}).
279 In the current study, given the radars narrow beam width and short wavelength, an approach solely
280 based on ρ_{HV} is used to filter sea-clutter. Since cross-correlation between horizontal and vertical
281 cross-polar received powers is largest for spherical hydrometeors, we label observations with
282 ρ_{HV} larger than a certain threshold as atmospheric returns and the rest as sea-clutter. The analysis
283 of a large sample of ρ_{HV} observations during clear and cloudy sky conditions indicates that the use
284 of a threshold of 0.9 for KaSACR2 and an average (over 5 range gates and 5 azimuthal
285 measurements) threshold of 0.55 for the XSAPR2 can be used to isolate hydrometeor-dominated
286 from clutter-dominated observations. The proposed ρ_{HV} technique successfully isolates
287 atmospheric returns at the same location for both the X-band at 1.0° elevation and the reference
288 Ka-band 0.5° elevation (Fig. 1b₂ and c₂ respectively; pink regions). However, it only identifies a
289 fraction of the atmospheric returns in the X-band 0.5° elevation observations. There, additional
290 filtering, beyond the scope of this study, would be required to suppress the remaining sea-clutter
291 and recover the missing atmospheric returns (see Moisseev and Chandrasekar, 2009; Unal, 2009
292 who propose advanced technique). Given this, XSAPR2 cross validation and precipitation rate
293 maps will be estimated using observations collected at 1.0° elevation since it offers the best
294 compromise between proximity to the surface and minimum sea-clutter contamination.
295

Deleted: -

297 **3.2 Radar Calibration**

298

299

300

301

302

303

304

305

306

307

308

309

310

311

312

313

314

315

316

317

318

319

320

321

322

323

324

325

326

327

328

329

330

331

332

333

334

335

336

337

338

339

340

341

342

Calibrated reflectivity observations are necessary to perform quantitative precipitation rate retrievals. Following Kollias et al. (2019), KAZR2 calibration is performed using collocated surface-based Parsivel laser disdrometer equivalent radar reflectivity estimates during light precipitation events as well as CloudSat observations collected over a small radius around the site. We estimate that, during the period of interest (01/10/2018 to 04/01/2018), KAZR2 radar reflectivity measurements are off by about +3-dB which we proceeded to correct for. The detailed time-series of KAZR2 calibration offset is presented in Fig. 2a.

Comparison of total (Fig. 3a) and range resolved (Fig. 3b) histograms of radar reflectivity measured by KAZR2 (pre-calibration) and KaSACR2 at zenith confirm that during the analysis period the KaSACR2 matched KAZR2. For this reason, KaSACR2 radar reflectivity measurements were also adjusted by the calibration constant depicted in Fig. 2a. Note how this comparison between the KAZR2 and KaSACR2 was performed between 1.5 to 5 km to avoid any differences in the reported radar reflectivities due to differences in how they detect ground/sea-clutter.

Calibrating the XSAPR2 radar reflectivity measurements is more challenging since it does not perform profiling observations and as such it cannot be benchmarked against disdrometer and KAZR2 observations. Performing a physical subsystem calibration remains the best way to calibrate the XSAPR2 system. Prior to the ACE-ENA field campaign (06/2017) the ARM engineering team performed such a procedure which is expected to bring the calibration of the XSAPR2 system used in this study to within 1 dB. Here, in an effort to develop alternative calibration/cross-validation methods, we also compare the XSAPR2 radar observations to Global Precipitation Measurement (GPM) Ku-band frequency of the Dual-frequency Precipitation Radar (DPR) observation when the satellite track crosses within a 245 km radius of the XSAPR2 radar site. It is not expected that both sets of observations will perfectly match because of the different footprints, path lengths and surface returns of both radars but this comparison should at least provide some insight in the event that the difference between both sensors is larger than several dB. For the comparison, the ground-based XSAPR2 reflectivity measurements are smoothed and interpolated to the satellite sampling volume: The azimuth-range measurements are smoothed using the 0.71° 3-dB beamwidth antenna weighting function of the GPM DPR (5-km footprint). Nearest neighbor is then used to match the satellite measurements in the horizontal plane while linear interpolation is used to match them in the vertical plane (Warren et al., 2018). Matched XSAPR2 radar reflectivity measurements are compared to GPM DPR corrected reflectivity measurements (GPM product version V06A Iguchi et al., 2010). Considering differences in radar sensitivity, radar reflectivity measurements with returns smaller than 14 dBZ are not considered during the comparison procedure (Toyoshima et al., 2015) and only periods when both radars coincidentally detect significant precipitation are used to perform calibration. For the analysis period, a total of 3 GPM overpasses with significant precipitation were observed for a total number of 1516 data points for the comparison.

An example of concurrent XSAPR2 and GPM DPR radar reflectivity observations are shown in Fig. 4a and c respectively. The example shows that both radars detected several shallow precipitation cells with cloud top heights between 3 and 4 km (Fig. 3b). Beyond agreeing in the

Deleted: to

Deleted: calibration

345 location of these precipitation echoes, both radars (XSAPR2 and GPM DPR) are found to agree
346 on their reflectivity intensity. To confirm their agreement, we estimated Contour of Frequency by
347 Altitude Diagram (CFAD) of the differences in radar reflectivities between the matched XSAPR2
348 and GPM DPR for all 1516 available observations (Fig. 4b). Above the height at which GPM DPR
349 is known to suffer from surface echo contamination (i.e., 1.5 km), the comparison between
350 XSAPR2 reflectivities and GPM DPR reflectivities shows no noticeable difference (i.e., no bias).
351 A scatter plot between the matched GPM DPR and XSAPR2 radar reflectivity for height above
352 1.5 km confirms the overall lack of bias beyond the expect 1 dB between the two radars at all
353 reflectivity (Fig. 4d on which the orange line depicts the best fit to the data and the dashed line
354 represent a perfect match between the datasets and the grey shading indicates the data density). As
355 mentioned above, scatter is expected because of the differences in configuration of both radar
356 systems. The cloud types present in the cases available could further enhance the impact of the
357 radar system differences since the shallow clouds observed during the 3 overpasses are of similar
358 or even smaller size compared to the GPM DPR footprint. Small clouds could lead to non-uniform
359 beam filling issue and as such to the GPM DPR underestimating the reflectivity of these cloud
360 system which could partially explain the seemingly “high” bias of the XSAPR2 in Fig. 4d.
361 Knowing that the ARM engineering team had calibrated the XSAPR2 just before the observations
362 used here were collected and because this comparison with the GPM DPR showed no bias larger
363 than several dB, we conclude that, for the observation period between 01/10/2018 to 04/01/2018,
364 the XSAPR2 was reasonably well calibrated and does not require any radar reflectivity
365 adjustments.

Deleted: ir

Deleted: location

Deleted: of these precipitation echoes

366 4.0 Radar Reflectivity-Based Precipitation Rate Retrievals

368 4.1 KAZR2

369
370
371 Intrieri et al. (1993) and later O'Connor et al. (2005) proposed a technique to constrain
372 water drop size distribution using lidar backscatter (related to water drop cross-section) and radar
373 Doppler spectral width (related to the width of the water drop size distribution). This radar-lidar
374 technique can be used to estimate precipitation rate at all levels in the subcloud layer when
375 collocated radar and ceilometer observations are available. We apply this technique to the
376 vertically pointing ceilometer lidar and KAZR2 pair operating at the ENA. The O'Connor et al.
377 (2005) technique requires ceilometer backscatter to be calibrated and remapped to the radar spatio-
378 temporal resolution (here 2 s x 30 m). Ceilometer backscatter is calibrated following a variation of
379 the O'Connor et al. (2004) technique by scaling observed path-integrated backscatter in thick
380 stratocumulus to match theoretical cloud lidar ratio values. Satisfactory conditions for ceilometer
381 backscatter calibration are identified as the first (in time) 20-min periods each day with standard
382 deviation of lidar ratio smaller than 1.5. The observed backscatter during the “satisfactory 20-min
383 period” are input to Hogan (2006)’s multi scattered model to determine a daily backscatter
384 calibration factor. For days where satisfactory conditions are not observed, a climatological
385 calibration factor of 1.35 is used to calibrate the observed backscatter. For the current analysis
386 period, the ceilometer backscatter calibration constant was estimated to vary around 1.35 +/- 0.08.
387 (Fig 2b). Calibrated ceilometer backscatter is subsequently mapped on the KAZR2 time-height
388 grid using a nearest neighbor approach.

Deleted: ¶

Distinct considerations must be taken to quantitatively retrieve precipitation rate from KAZR2, XSAPR2 and KaSACR2 measurements. ¶

389 This radar-lidar technique generates time-height maps of precipitation rate from 200 m above
390

398 ground level to 90 m below cloud base height which are filtered for aerosol contamination. We
399 use the clear-sky – according to KAZR - calibrated lidar backscatter signals as a reference for
400 aerosol behavior. Lidar calibrated backscatter values below the mean clear-sky calibrated
401 backscatter value at each height, depicted as the black vertical line in Fig. 2c, are systematically
402 removed from the analysis to leave only drizzle signals. In addition, to aerosol contaminated
403 returns, unphysical values with median diameter smaller than 10 μ m or equal or large to 1000 μ
404 m are also removed from our analysis.

405
406 Two one-hour examples of cloud location (black dots) and precipitation rate estimated using
407 this technique are shown in Fig. 5a and b. Because of evaporation, the most intense
408 precipitation rates are observed near cloud base height and a significant fraction of the
409 precipitation does not reach the surface and falls as virga.

411 4.2 XSAPR2

412
413 As previously mentioned, the estimation of the precipitation rate for the XSAPR2 i) cannot
414 depend on the use of polarimetric observations, because of the absence of polarimetric signature
415 from spherical drizzle drops and ii) cannot depend on the use of disdrometer-based estimates of
416 the relationship between the radar reflectivity (Z) and the precipitation rate (R), because
417 observations collected at the surface may not be representative of other levels in the subcloud layer
418 especially at the ENA where evaporation is an active process.

419
420 To accommodate changes in drizzle drop size distribution with height which could be associate
421 for example to changes in aerosol loading or evaporation, we propose to construct adaptive (both
422 with time and height) Z - R relationships in the form $Z = \alpha R^\beta$ from precipitation rates retrieved
423 through the KAZR-ceilometer technique (see section 4.1). Every 30 min, independently for every
424 level in the subcloud layer, retrieved zenith precipitation rates (R in mm hr^{-1}) and calibrated KAZR
425 reflectivity (Z in $\text{mm}^6 \text{m}^{-3}$) reported during a 12-h window around that time are related through the
426 relationship:

$$427 \log_{10}(Z) = \log_{10}(\alpha) + \beta \cdot \log_{10}(R) \quad (1)$$

428
429 The prefactor α and exponent β are estimated using a total least square regression technique only
430 considering R between $10^{-3.5}$ and $10^{0.5}$ mm hr^{-1} and only if at least 350 precipitation detections are
431 available. When too few observations are available, average (for the period of the current study)
432 α and β are used. A 12h time window was determined to be the best compromise between data
433 density and least change in water drop size distribution characteristics.

434
435 To evaluate the adaptive Z - R , we apply three different precipitation retrieval techniques to
436 KAZR2 reflectivity observations: We compare precipitation rate statistics retrieved following
437 the O'Connor et al. (2005) technique (ideal technique, red), to those estimated using Z - R
438 relationships constructed using fixed (approach proposed by Comstock et al. (2004), green) or
439 adaptive (approach proposed here, black) coefficients (presented in Fig. 6e and f respective).
440 Figure 6f shows that the proposed adaptive Z - R relationships can reproduce the precipitation
441 rate statistics obtained using the ideal O'Connor et al. (2005) technique. The same cannot be
442 said from using traditional fixed Z - R relationships such as that proposed by Comstock et al.
443

Deleted: ,

Deleted: l

Deleted: addition

Deleted: al

448 (2004) which tends to create an underestimation of precipitation intensity (Fig. 6e).

449

450 Fig. 6a and b respectively present time series of α and β near cloud base (i.e., 90 m below
451 cloud base height) for a 30-day long period that overlaps with the second phase of the ACE-
452 ENA field campaign: Again for comparison we illustrate our adaptive coefficients (black), the
453 Comstock et al. (2004) constant coefficients (dashed green) and coefficients estimated from
454 surface-based Parsivel laser disdrometer measurements (dashed orange). The gradual increase
455 in both the adaptive α and β coefficients over time is consistent with reports of observed
456 conditions indicating a transition from shallow precipitation at the end of January to deep
457 frontal precipitation at the end of February. CFADs of α and β (Fig. 6c and d respectively)
458 show how the adaptive α additionally has a tendency to increase with distance from cloud base
459 (from top to bottom), which is consistent with the evaporation of small drops that leads to an
460 increase in mean drop size and has been previously reported by Comstock et al. (2004) and
461 discussed in VanZanten et al. (2005).

462

463 Figure 5c and d show how, by applying the adaptive Z-R, XSAPR2 reflectivity observations
464 collected at 1° elevation can be converted to precipitation rate. Note how the adaptive Z-R
465 relationships were directly applied to clutter-filtered calibrated XSAPR2 radar reflectivity
466 measurements since we estimate that, for the majority of the conditions occurring at the ENA
467 observatory, both two-way gas attenuation and liquid attenuation at X-band are negligible.
468 According to Rosenkranz (1998), at X-band frequency, gas attenuation generally amounts to 0.03
469 dB km⁻¹ which is much smaller than even the radar calibration uncertainty. Similarly, Matrosov et
470 al. (2005) discusses how, for rain rates of 2 mm hr⁻¹, liquid attenuation roughly amounts to 0.015
471 dB km⁻¹ which over the depth of the shallow systems producing this type of precipitation cumulates
472 to liquid attenuation less than 1 dB again within the radar calibration uncertainty. We do however
473 acknowledge that, for deep convective systems, liquid attenuation correction would be granted,
474 but since this type of precipitating system was not being frequently observed at the ENA
475 observatory, we did not apply any liquid attenuation correction to the XSAPR2 measurements.

476

477 4.3 KaSACR2

478

479 Before quantitatively estimating precipitation rate from KaSACR radar reflectivity
480 measurements, we also consider how its wavelength responds to the presence of atmospheric
481 gases. Rosenkranz (1998) propagation model suggests that, for the conditions observed at the
482 ENA, two-way gas attenuation of Ka-band signals can amount to 0.25 dB km⁻¹. Although this may
483 seem small and can be insignificant when collecting observations of boundary layer clouds in
484 profiling mode, in scan mode, attenuation of Ka-band reflectivity by atmospheric gas can amount
485 to 10 dB at 40 km range (Fig. 7b, difference between the black and green curve) and as such
486 should not be neglected. Also note that in addition to the gaseous attenuation, Ka-band radars
487 suffer from considerable liquid water attenuation. According to Matrosov (2005), the
488 relationship between one way liquid attenuation a (dB km⁻¹) and precipitation rate R (mm hr⁻¹)
489 is very robust ($a = 0.28R$). His findings were verified using Mie scattering calculations on
490 all particle size distributions observed by the ENA Parsivel laser disdrometer. The top panels
491 of Fig. 8 illustrates an example of observations collected by the KaSACR at 0.5 elevation on
492 02/13/2018. In this example, liquid contributed anywhere from 2 to 10 dB in total attenuation
493 at Ka-band over the 40 km observation domain (Fig. 8e). If left uncorrected, liquid attenuation

Deleted: can be

Deleted: is

Deleted: (generally amounts to 0.03 dB km⁻¹ according to

Deleted: .

Deleted: 9

Deleted: 7e

Deleted: ,

Deleted: i

502 can lead to errors in precipitation rate estimates up to 3 mm hr⁻¹ in this example (Fig. 6f). The
503 bottom panels of Fig. 8 also shows reflectivity and precipitation rate for the XSAPR2 which,
504 as discussed in the previous section, only suffers from negligible attenuation. With the caveat
505 that we are comparing rain rates retrieved at slightly different slanted elevations, comparing
506 rain rates retrieved from the XSAPR2 observations (Fig. 8h) and from the KaSACR2
507 observations corrected for both gas and liquid attenuation (Fig. 8d) also highlights the fact that
508 even after all correction are performed the KaSACR2 “realized” sensitivity does not allow it
509 to detect some of the precipitation the more sensitive XSAPR2 can detect. The range-
510 dependent sensitivity of both sensors can be contrasted in Fig. 7b.

512 5.0 Complementary of different radar systems in Characterizing Light Precipitation 513 Variability

514
515 As discussed in section 2.0, the KAZR2, KaSACR2 and XSAPR2 radars sample light
516 precipitation using very different transmission and sampling strategies. In this section we highlight
517 some of the advantages and tradeoffs of using each radar system to characterize different aspects
518 of light precipitation variability.

519 First constrasting the two scanning radar XSAPR2 and KaSACR2. Although the Ka-band
520 SACR2 experiences less sea-clutter than the X-band SAPR2, because of needs for cloud
521 sampling, it only currently performs one PPI scan at 0.5° every 15 min which limits its
522 temporal resolution. In addition, based on their technical specifications (Table 1), the XSAPR2
523 single pulse radar sensitivity is approximately 10 dB higher than that of the KaSACR2 (Fig. 7b
524 blue and black line respectively). Finally, the Ka-band SACR2 also suffer from significantly more
525 attenuation from atmospheric gases (Fig. 7b green line) and liquid water which even if corrected
526 for still decrease it’s “realized” sensitivity. For all these reasons, we conclude that the XSAPR2
527 is more suitable for characterizing light precipitation variability over large domains.

528
529 Second, to contrast the XSAPR2 and KAZR2, we compare, over the course of 36 hours between
530 00:00 UTC February 2 and 12:00 UTC February 3, hourly precipitation rate variability in the forms
531 of frequency of occurrence in different precipitation rate bins (pdf). Figure 9a shows estimates
532 from the scanning XSAPR2 collecting observation in PPI mode covering a domain between 2.5
533 and 40 km at 1° elevation thus transecting heights between ~100 m and 750 m (also refer to Fig.
534 7a to visualize the XSAPR2 sampling geometry). Figure 9b and c respectively show estimates
535 from the vertically pointing KAZR2 200 m above the surface and 90 m below cloud base which
536 was around 850 m.

537
538
539 From Fig. 9b and c, it is evident that KAZR2, with its high sensitivity, is especially well suited to
540 document light precipitation and drizzle falling at a rate as low as 10⁻⁴ mm hr⁻¹. KAZR2
541 observations show a reduction in the number of precipitation events and in precipitation intensity
542 from cloud base (Fig. 9c) towards the surface (Fig. 9b). This supports previous hypothesis that at
543 the ENA a large fraction of the light precipitation falls in the form of virga (Ahlgren and Forbes,
544 2014; Yang et al., 2018). Under these circumstances, where the character of precipitation changes
545 dramatically with height and its intensity is very low (below 10⁻³ mmhr⁻¹), scanning radar
546 observation at a fixed elevation may become inadequate to characterize surface precipitation over
547 a large domain owing to Earth curvature effects. Fig. 7a illustrates the height above the surface of

- Deleted: 6
- Deleted: (Fig 6g and h)
- Deleted: C
- Deleted: observations
- Deleted: unattenuated
- Deleted: 6h
- Deleted: observations
- Deleted: 6
- Deleted: 9
- Deleted: c

- Commented [LK1]: Moved from the end to the begging of this section.
- Deleted: For illustration purposes,
- Deleted: 8
- Deleted: 9
- Deleted: 8
- Deleted: 8
- Deleted: 8
- Deleted: 8
- Deleted: 9

566 a 1° elevation scan with distance away from the radar; at a distance of 10-20 km the radar beam is
567 already 250 m above the surface while at a distance of 20-30 km this same radar beam is now 500
568 m from the surface. This non-uniformity of the radar beam height with distance makes scanning
569 cloud radar observations at one elevation angle more adequate to document the character of
570 vertically uniform precipitation. The rapid sampling rate of the KAZR2 also allows it to describe
571 the vertical structure of precipitation variability at a high temporal (scales as short as 2s).
572

573 On the other hand, one drawback of vertically pointing KAZR2 observations is that they are limited
574 to sampling only those precipitation events advected overhead. It is not uncommon to temporally
575 average vertically pointing observation to create a proxy for domain average statistics, however as
576 depicted in Fig. 5 it may be difficult to address the domain representativeness of one-hour of
577 vertically pointing precipitation rate estimates. It can also be challenging to interpret the mesoscale
578 organization of the precipitation field using vertically pointing observations alone; Scanning
579 systems such as the XSAPR2 can help fill this gap. Figure 5c and d show XSAPR2 1° elevation
580 PPI scans collected at 10:00 am and 8:00 am respectively which corresponds to the center time of
581 the KAZR2 time-height observations presented in Fig. 5a and b. XSAPR2 can observe the
582 structure and scales of popcorn precipitation and squall line precipitation over a domain of roughly
583 2,500 km². In its current configuration, the XSAPR2 system can be used to document the
584 horizontal structure and temporal variability of light-to-moderate precipitation on scales of ~5
585 minutes. Referring back to Fig. 9a hourly precipitation rate pdfs, it is evident that by covering a
586 larger domain XSAPR2 is able to observe a larger number of near surface sporadic precipitation
587 events such as that observed on Feb 03 around 0:00 and of isolated deep convective events
588 responsible for more intense precipitation ($R > 3 \text{ mm hr}^{-1}$) such as that observed on Feb 03 around
589 8:00.
590

592 6.0 Gridded Domain Precipitation Rate Estimation

593
594 One way for scanning radars to overcome some of the limitation of their scanning strategy
595 is to develop horizontal, two-dimensional, gridded maps of the radar observables and other
596 quantities (i.e. precipitation rate) using measurements collected at different elevations angles (i.e.,
597 construct constant altitude plan position indicator (CAPPI) maps). Here, gridded XSAPR2
598 CAPPI's are constructed as follows: We perform the polar to Cartesian transformation for each
599 individual reflectivity measurement using a standard atmosphere radio propagation model which
600 considers the height of the beam above the Earth surface, and the distance between the radar and
601 the projection of the beam along the Earth surface (Doviak and Zrníc, 1993). Using these Cartesian
602 coordinates each PPI is mapped on a 100 m horizontal grid for which each grid point is populated
603 using a triangulation technique (i.e., the nearest three observations are linearly interpolated to
604 populate the grid cell). Then, every 100 m in the horizontal, a grid point at constant altitude is
605 populated by i) a measured value if falling on an elevation where observations were collected or
606 otherwise ii) a weighted average of the gridded data from the three closest PPI; The weight being
607 the inverse horizontal distance from the grid location. The aforementioned adaptive Z-R
608 relationships are then applied to the Cartesian grid reflectivity observations to produce
609 precipitation rate CAPPI. Note that producing an unbiased assessment of precipitation rate over
610 the domain covered by the scanning radar would require the application of a uniform sensitivity
611 threshold over the entire domain. The need for such a threshold creates a tradeoff between

Deleted: 8

Deleted: such as the one illustrated in Fig. 9b. Figure 9 shows a Cartesian coordinate constant altitude plan position indicator (CAPPI) map of precipitation rate constructed around an altitude of 500 m using XSAPR2 observations collected between 1 and 5° elevation (Fig. 9a, red color). This figure also illustrates how scanning radar sensitivity is range dependent such that weak precipitation rates can only be detected close to the sensor (Fig. 9b light grey colors).

Deleted: P

Deleted: ing

Deleted: s

Deleted: observed by the scanning radar which

625 documenting a large domain and documenting weak precipitation events. As quantified in Fig. 7b,
626 at a distance of 40 km the XSAPR2 is only capable of detecting precipitation events of intensity
627 larger than $10^{-2.8}$ mm hr⁻¹ and any desire to document weaker precipitation rate events would
628 further limit domain size.

Deleted: 9

Deleted: c

630 7.0 Domain Average Precipitation Rate - When do Temporal and Horizontal Precipitation 631 Variability Converge? 632

633 The addition of the XSAPR2 at the ENA observatory offers new insights into precipitation
634 variability and organization over a domain of 40-60 km radius around the site. However, the
635 XSAPR2 data record is not as long as the KAZR data record which now spans 5 years at the ENA
636 even totaling up to 7.5 years if we consider the Cloud, Aerosols, and Precipitation in the Marine
637 Boundary Layer (CAP-MBL) campaign that took place at the site from April 2009 until January
638 2011 (Wood et al., 2005). Because of their longer data record, profiling radar observations have
639 the potential to inform us about decadal precipitation variability both temporal and structural.
640 However, with vertically pointing observations, it is near impossible to disentangle temporal
641 evolution from horizontal structure. Classical approaches rely on Taylor hypothesis of frozen
642 turbulence to convert elapsed time to horizontal dimension using the horizontal wind speed
643 responsible for advecting cloud and precipitation overhead. While widely used, little research has
644 been conducted to determine the validity and limitations of this assumption (see Oue et al. (2016)
645 for a discussion on cloud fraction). In this section we seek to determine how long does one need
646 to observe precipitation advected overhead to gather statistical precipitation information
647 equivalent to that of a 40 km radius domain.
648

Deleted: 80

Deleted: wide

649 Over the 3-month period between 01/10/2018 and 04/01/2018, the domain representativeness of
650 KAZR2 precipitation rate estimates is evaluated using XSAPR2 observations collected over a
651 domain of 40 km radius around the site. Although any height could be used, we perform this
652 comparison at the specific height of 500 m: While KAZR2 precipitation retrievals can be directly
653 extracted at 500 m, those from XSAPR2 must be extracted from gridded CAPPI fields which are
654 constructed following the details provided in Section 6 using a collection of PPI scans. To remove
655 any bias caused by variations in minimum performance of both sensors, a minimum precipitation
656 rate threshold of $10^{-2.8}$ mm hr⁻¹ is applied to both sensors reflecting the detectability of the XSAPR2
657 over the selected domain. Statistics for both sensors are estimated using different set averaging
658 time intervals (30 min, 1 h, 3 h, 12 h and 24 h) which allows us to monitor the temporal variability
659 of domain-average precipitation rate. For XSAPR2, using a sliding window, we average all 5-min
660 PPI observations collected during the chosen time interval. For KAZR, we center the time window
661 on the XSAPR2 estimates and average all 2-s observations collected during the chosen time
662 interval.
663

Deleted: P

Deleted: reported by

Deleted: at 1° elevation are used to evaluate the representativeness of KAZR2 observations collected 200 m above the surface

664 Figure 10 shows the precipitation rate pdfs estimated from the XSAPR2 (blue) and KAZR2 (red)
665 for varying averaging time interval. Focusing on features such as the width, the minimum,
666 maximum and modes of the precipitation rate statistical distribution; Results indicate that neither
667 30 min nor 1h averaging of KAZR precipitation rate estimates can be used to replicate the
668 precipitation rate statistics corresponding to those of domain averaged over 30 min (Fig. 10 left
669 column). Averaging of 3 hours of KAZR2 data improves its representativeness of domain average
670 rain rate variabilities on scales of 1 to 3-hrs (2nd and 3rd rows/3rd column). Convergence between

Deleted:

Deleted: Figure 10's 3rd and 4th columns/3rd and 4th rows, suggests that longer time averages (3h and 12 h) of KAZR2 observations capture the most frequently occurring precipitation mode of domain-average precipitation rate on 3h and 12 h timescales.

686 XSAPR2 and KAZR2 time-average precipitation rate estimates is seemingly best when
687 considering the variability of domain-average precipitation rate over 12 h (correlation coefficient
688 R=0.25) or longer timescales; 12-h average domain-average precipitation rate pdf from XSAPR2
689 and 12-h average precipitation rate pdf from KAZR are similar in both magnitude and mode
690 location.

691
692 Although these results are estimated with few observational cases (3 month period), they clearly
693 suggest that XSAPR2 observations are necessary to characterize short-term (< 1 h) domain-
694 average precipitation rate characteristics. They also suggest that longer-term (12 h) domain-
695 average precipitation rate characteristics can be estimated by averaging either XSAPR2 or KAZR2
696 observations using time-windows of similar lengths.

697 8.0 Summary and Conclusions

698
699 The ARM ENA observatory is the first island-based climate research facility equipped with
700 collocated radars and lidars capable of sampling light oceanic precipitation. Here we presented the
701 characteristics and first light observations from three state-of-the-art 2nd generation radar systems:
702 The Ka-band Zenith radar (KAZR2), the Ka-band scanning ARM cloud radar (KaSACR2) and the
703 X-band scanning ARM precipitation radar (XSAPR2),
704

705
706 One of the initial concerns of operating scanning cloud and precipitation radars over the ocean is
707 the impact of sea-clutter, especially at low-elevation angles. Nearly one hundred hours of clear sky
708 observations were used to characterize the properties of sea-clutter in KaSACR2 and XSAPR2
709 observations. Analysis of clear and cloudy skies periods and intercomparison of the meteorological
710 and non-meteorological echoes of the KaSACR2 made it possible to design a relatively simple
711 filtering technique to isolate precipitation echoes in XSAPR2 observations. In short, a threshold
712 on normalized coherent power (< 0.3) and on average (5x5 window) cross-correlation (< 0.55),
713 can mitigate second-trip echoes and sea-clutter echoes. Everything considered, we find that
714 XSAPR2 observations collected at 1° elevation, albeit suffering from more clutter contamination
715 than KaSACR2, offer the best compromise between clutter contamination and proximity to the
716 surface.

717
718 Measurement calibration is also essential to quantitative precipitation rate retrieval. We applied
719 the Kollias et al. (2019) technique to calibrate the KAZR2 radar reflectivity measurements using
720 Parsivel disdrometer and CloudSat observations. Because they were found to match, the same
721 offset is applied to the KaSACR2 observations. To confirm the recent calibration performed by
722 the ARM engineering team and to explore alternative calibration methods, the XSAPR2
723 reflectivity measurements were statistically compared to GPM Ku-band radar observations
724 collected around the ENA site. The analysis indicated no noticeable offset; thus, no calibration
725 offset was applied to the XSAPR2. These techniques could be used in the future as a supplement
726 to the ARM radar engineering group efforts to characterize the ENA radars reflectivity
727 measurements.

728
729 We capitalized on the availability of closely collected (in both time and physical distance) KAZR2,
730 ceilometer lidar and XSAPR2 measurement to estimate precipitation rate. Precipitation rates
731 retrieved using the O'Connor et al. (2005) radar-lidar technique have the advantage of being

Deleted: (in terms of root mean square error (RMSE))

Deleted: timescales of

Deleted: RMSE

Deleted: 13.4%

Deleted:

Deleted: 0

Deleted: days

Deleted: 3

Deleted: the

Deleted:

Deleted: calibrate

Deleted: we relied on a

Deleted: ison

Deleted: with

746 estimated with fewer assumptions on the drizzle drop size distribution and can accommodate
747 changes in aerosol loading, liquid water path and evaporation. Unfortunately, for a lack of scanning
748 lidar observations, we cannot apply this technique to scanning radar observations. Instead, we
749 showed how relating the retrieved precipitation rates in the column to radar reflectivity can be used
750 to estimate adaptive (in both time and height) parameters that related observed radar reflectivity
751 (Z) to precipitation rate (R) in the form $Z = \alpha R^\beta$. These adaptive parameters can then be applied
752 to retrieve precipitation rate over the domain covered by scanning cloud radars. We report these
753 adaptive parameters for the period between 01/10/2018 and 04/01/2018 which includes the second
754 phase of the ACE-ENA campaign. These adaptive parameters were shown to capture changes in
755 drop size distribution with height as well as temporal changes in the cloud field.

756
757 Throughout this work, comparison of precipitation rate statistics estimated by all three sensors
758 highlighted the following:

- 759 1) Because of strong signal attenuation by gases and liquid at Ka-band, X-band radars are
760 more suited for precipitation mapping especially over large domains.
- 761 2) When the character of precipitation varies rapidly with height for instance owing to an
762 active evaporation process, zenith-pointing radars are more suited for precipitation
763 characterization;
- 764 3) However, zenith-pointing observations collected over periods shorter than 12h should not
765 be considered representative of a domain especially one as large as 2,500 km² (i.e., ~40 km
766 radius half circle).
- 767 4) When it comes to capturing the general shape of the precipitation rate distribution, 12-hrs
768 of zenith-pointing radar observations can be averaged to represent the 12-h variability of
769 such a ~40 km radius half circle domain.
- 770 5) Shorter term domain precipitation rate variability can only be capture by scanning
771 precipitation radars and especially those operating at weakly-attenuating frequencies and
772 with high sensitivity such as the XSAPR2.
- 773 6) Scanning sensors such as the XSAPR2 are also better suited to document sporadic and
774 horizontal homogeneous precipitation including precipitation presenting mesoscale
775 organization.
776

777
778 In a nutshell, the considerable differences in precipitation rate statistics estimated by the XSAPR2
779 and KAZR2 challenge our ability to objectively estimate precipitation rate statistics over a domain
780 for applications such as evaluation of high-temporal resolution model output. Factors such as
781 instrument sensitivity, sampling resolution, sampling height and domain size should always be
782 considered when comparing model output to observations. One way to consider these factors could
783 be to convert model output rain rates to observable rain rate through the use of forward simulators
784 which can use drop size and atmospheric conditions information to reproduce the attenuation
785 affecting radar signals. Several forward-simulator further take into consideration the dependency
786 of radar sensitivity with range which dictates the minimum detectable rain rate at various distance
787 within a domain (e.g., Tatarevic et al., 2015; Lamer et al., 2018).

Deleted: without

Deleted: shape

Deleted: which can

Deleted: f

Deleted: ed

Deleted: ng

Deleted: Estimates of

Deleted:

Deleted: precipitation rate variability on timescale of 12 hours can be captured by averaging 12h of zenith-pointing radar observations collected at 200 m above the surface

Deleted: .

Deleted: temporal

Deleted: for example through the use of

Deleted: forward simulators.

807 **Authors contributions**

808

809 K. Lamer coordinated the project, performed the intercomparisons between the
810 precipitation rates produced by the three radars and produced the final manuscript draft. P. Kollias
811 supervised Z. Zhu and B. Puigdomènech Treserras as they respectively analyzed the KAZR2 and
812 both the KaSACR2 and XSAPR2 observations; Analysis steps included performing data post-
813 processing, calibration and precipitation rate retrievals. B. Puigdomènech Treserras also produced
814 the CAPPI part of this work. B. Isom and N. Bharadwaj provided a wealth of information about
815 the radar system characteristics as well as guidance on radar data calibration. All coauthors have
816 read the manuscript draft and have contributed comments.

817 **Acknowledgments**

818

819 K. Lamer contributions were supported by subcontract 300324 of the Pennsylvania State
820 University with the Brookhaven National Laboratory in support to the U.S. Department of Energy
821 (DOE) ARM-Atmospheric Science Research (ASR) Radar Science group. B. Puigdomènech
822 Treserras contributions were supported through a subcontract with the Brookhaven National
823 Laboratory in support to the ARM-ASR Radar Science group. Z. Zhu contributions were supported
824 by the U.S. DOE ASR ENA Site Science award. B. Isom and N. Bharadwaj contributions were
825 supported by Pacific North West National Laboratory. P. Kollias contributions were supported by
826 the U.S. DOE under Contract DE-SC0012704.

827

828 **Data availability**

829

830 All ARM data streams are available online at: <http://www.archive.arm.gov/discovery/>. All
831 GPM data streams are available online at <https://pmm.nasa.gov/data-access/downloads/gpm>.

832

833

834

835

836

837

838

839

840

841

842

843

844

845

846

847

848

849

850

851

852

Deleted: ¶

854 **References**

855

856 Adler, R. F., Wang, J.-J., Gu, G., and Huffman, G. J.: A ten-year tropical rainfall climatology based
857 on a composite of TRMM products, *Journal of the Meteorological Society of Japan. Ser.*
858 *II*, 87, 281-293, 2009.

859 Ahlgrimm, M., and Forbes, R.: Improving the representation of low clouds and drizzle in the
860 ECMWF model based on ARM observations from the Azores, *Monthly Weather Review*,
861 142, 668-685, 2014.

862 Alku, L., Moisseev, D., Aittomäki, T., and Chandrasekar, V.: Identification and suppression of
863 nonmeteorological echoes using spectral polarimetric processing, *IEEE Transactions on*
864 *Geoscience and Remote Sensing*, 53, 3628-3638, 2015.

865 Bretherton, C. S., Uttal, T., Fairall, C. W., Yuter, S. E., Weller, R. A., Baumgardner, D., Comstock,
866 K., Wood, R., and Raga, G. B.: The EPIC 2001 stratocumulus study, *Bulletin of the*
867 *American Meteorological Society*, 85, 967-978, 2004.

868 Comstock, K. K., Wood, R., Yuter, S. E., and Bretherton, C. S.: Reflectivity and rain rate in and
869 below drizzling stratocumulus, *Quarterly Journal of the Royal Meteorological Society*,
870 130, 2891-2918, 2004.

871 Comstock, K. K., Bretherton, C. S., and Yuter, S. E.: Mesoscale variability and drizzle in southeast
872 Pacific stratocumulus, *Journal of the Atmospheric Sciences*, 62, 3792-3807, 2005.

873 Doviak, R., and Zrnic, D.: *Doppler Radar and*, 1993.

874 Ellis, T. D., L'Ecuyer, T., Haynes, J. M., and Stephens, G. L.: How often does it rain over the
875 global oceans? The perspective from CloudSat, *Geophysical Research Letters*, 36, 2009.

876 Feingold, G., Koren, I., Wang, H., Xue, H., and Brewer, W. A.: Precipitation-generated
877 oscillations in open cellular cloud fields, *Nature*, 466, 849, 2010.

878 Gorgucci, E., Scarchilli, G., and Chandrasekar, V.: Sensitivity of multiparameter radar rainfall
879 algorithms, *Journal of Geophysical Research: Atmospheres*, 105, 2215-2223, 2000.

880 Gregers-Hansen, V., and Mital, R.: An empirical sea clutter model for low grazing angles, *Radar*
881 *Conference, 2009 IEEE*, 2009, 1-5.

882 Hogan, R. J.: Fast approximate calculation of multiply scattered lidar returns, *Applied Optics*, 45,
883 5984-5992, 2006.

884 Horst, M., Dyer, F., and Tuley, M.: Radar sea clutter model, *Antennas and Propagation*, 1978, 6-
885 10.

886 Iguchi, T., Seto, S., Meneghini, R., Yoshida, N., Awaka, J., and Kubota, T.: GPM/DPR level-2
887 algorithm theoretical basis document, NASA Goddard Space Flight Center, Greenbelt,
888 MD, USA, Tech. Rep. 2010.

889 Intrieri, J. M., Stephens, G. L., Eberhard, W. L., and Uttal, T.: A method for determining cirrus
890 cloud particle sizes using lidar and radar backscatter technique, *Journal of Applied*
891 *Meteorology*, 32, 1074-1082, 1993.

892 Kollias, P., Bharadwaj, N., Widener, K., Jo, I., and Johnson, K.: Scanning ARM cloud radars. Part
893 I: Operational sampling strategies, *Journal of Atmospheric and Oceanic Technology*, 31,
894 569-582, 2014a.

895 Kollias, P., Jo, I., Borque, P., Tatarevic, A., Lamer, K., Bharadwaj, N., Widener, K., Johnson, K.,
896 and Clothiaux, E. E.: Scanning ARM cloud radars. Part II: Data quality control and
897 processing, *Journal of Atmospheric Oceanic Technology*, 31, 583-598, 2014b.

898 Kollias, P., Clothiaux, E. E., Ackerman, T. P., Albrecht, B. A., Widener, K. B., Moran, K. P.,
899 Luke, E. P., Johnson, K. L., Bharadwaj, N., and Mead, J. B.: Development and applications
900 of ARM millimeter-wavelength cloud radars, *Meteorological Monographs*, 57, 17.11-
901 17.19, 2016.

902 Kollias, P., Puigdomènech Treserras, B., and Protat, A.: Calibration of the 2007-2017 record of
903 ARM Cloud Radar Observations using CloudSat, *Atmos. Meas. Tech. Discuss.*, 2019, 1-
904 30, 10.5194/amt-2019-34, 2019.

905 Lamer, K., Fridlind, A. M., Ackerman, A. S., Kollias, P., Clothiaux, E. E., & Kelley, M.: (GO)²-
906 SIM: a GCM-oriented ground-observation forward-simulator framework for objective
907 evaluation of cloud and precipitation phase. *Geoscientific Model Development*, 11(10),
908 4195-4214. 2018
909

910 Lamer, K., Kollias, P., and Nuijens, L.: Observations of the variability of shallow trade wind
911 cumulus cloudiness and mass flux, *Journal of Geophysical Research: Atmospheres*, 120,
912 6161-6178, 2015.

913 Luke, E. P., Kollias, P., Johnson, K. L., and Clothiaux, E. E.: A technique for the automatic
914 detection of insect clutter in cloud radar returns, *Journal of Atmospheric and Oceanic*
915 *Technology*, 25, 1498-1513, 2008.

916 Mather, J., Turner, D., and Ackerman, T.: Scientific maturation of the ARM Program,
917 *Meteorological Monographs*, 57, 4.1-4.19, 2016.

918 Matrosov, S. Y.: Attenuation-based estimates of rainfall rates aloft with vertically pointing Ka-
919 band radars, *Journal of Atmospheric and Oceanic Technology*, 22, 43-54, 2005.

920 Matrosov, S. Y., Kingsmill, D. E., Martner, B. E., & Ralph, F. M.: The utility of X-band
921 polarimetric radar for quantitative estimates of rainfall parameters. *Journal of*
922 *hydrometeorology*, 6(3), 248-262, 2005
923

924 Miller, M., and Yuter, S.: Detection and characterization of heavy drizzle cells within subtropical
925 marine stratocumulus using AMSR-E 89-GHz passive microwave measurements,
926 Atmospheric Measurement Techniques, 6, 1-13, 2013.

927 Moisseev, D. N., and Chandrasekar, V.: Polarimetric spectral filter for adaptive clutter and noise
928 suppression, Journal of Atmospheric and Oceanic Technology, 26, 215-228, 2009.

929 Moyer, K. A., and Young, G. S.: Observations of mesoscale cellular convection from the marine
930 stratocumulus phase of “FIRE”, Boundary-Layer Meteorology, 71, 109-133, 1994.

931 Nathanson, F. E., Reilly, J. P., and Cohen, M. N.: Radar design principles-Signal processing and
932 the Environment, NASA STI/Recon Technical Report A, 91, 1991.

933 Nguyen, C. M., Moisseev, D. N., and Chandrasekar, V.: A parametric time domain method for
934 spectral moment estimation and clutter mitigation for weather radars, Journal of
935 Atmospheric and Oceanic Technology, 25, 83-92, 2008.

936 O'Connor, E. J., Illingworth, A. J., and Hogan, R. J.: A technique for autocalibration of cloud lidar,
937 Journal of Atmospheric and Oceanic Technology, 21, 777-786, 2004.

938 O'Connor, E. J., Hogan, R. J., and Illingworth, A. J.: Retrieving stratocumulus drizzle parameters
939 using Doppler radar and lidar, Journal of Applied Meteorology, 44, 14-27, 2005.

940 Oue, M., Kollias, P., North, K. W., Tatarevic, A., Endo, S., Vogelmann, A. M., and Gustafson, W.
941 I.: Estimation of cloud fraction profile in shallow convection using a scanning cloud radar,
942 Geophysical Research Letters, 43, 2016.

943 Paluch, I., and Lenschow, D.: Stratiform cloud formation in the marine boundary layer, Journal of
944 the atmospheric sciences, 48, 2141-2158, 1991.

945 Pazmany, A. L., Mead, J. B., Bluestein, H. B., Snyder, J. C., and Houser, J. B.: A mobile rapid-
946 scanning X-band polarimetric (RaXPoL) Doppler radar system, Journal of Atmospheric and
947 Oceanic Technology, 30, 1398-1413, 2013.

948 Rapp, A. D., Lebsock, M., and L'Ecuyer, T.: Low cloud precipitation climatology in the
949 southeastern Pacific marine stratocumulus region using CloudSat, Environmental Research
950 Letters, 8, 014027, 2013.

951 Rauber, R. M., Stevens, B., Ochs III, H. T., Knight, C., Albrecht, B. A., Blyth, A., Fairall, C.,
952 Jensen, J., Lasher-Trapp, S., and Mayol-Bracero, O.: Rain in shallow cumulus over the
953 ocean: The RICO campaign, Bulletin of the American Meteorological Society, 88, 1912-
954 1928, 2007.

955 Rémillard, J., and Tselioudis, G.: Cloud regime variability over the Azores and its application to
956 climate model evaluation, Journal of Climate, 28, 9707-9720, 2015.

957 Rosenkranz, P. W.: Water vapor microwave continuum absorption: A comparison of
958 measurements and models, Radio Science, 33, 919-928, 1998.

- 959 Ryzhkov, A., Zhang, P., Doviak, R., and Kessinger, C.: Discrimination between weather and sea
 960 clutter using Doppler and dual-polarization weather radars, Proc. 27th General Assembly
 961 of the International Union of Radio Science, 3, 2002.
- 962 Savic-Jovicic, V., and Stevens, B.: The structure and mesoscale organization of precipitating
 963 stratocumulus, *Journal of the Atmospheric Sciences*, 65, 1587-1605, 2008.
- 964 Schumacher, C., and Houze Jr, R. A.: Comparison of radar data from the TRMM satellite and
 965 Kwajalein oceanic validation site, *Journal of Applied Meteorology*, 39, 2151-2164, 2000.
- 966 Sharon, T. M., Albrecht, B. A., Jonsson, H. H., Minnis, P., Khaiyer, M. M., van Reken, T. M.,
 967 Seinfeld, J., and Flagan, R.: Aerosol and cloud microphysical characteristics of rifts and
 968 gradients in maritime stratocumulus clouds, *Journal of the Atmospheric Sciences*, 63, 983-
 969 997, 2006.
- 970 Siggia, A., and Passarelli, R.: Gaussian model adaptive processing (GMAP) for improved ground
 971 clutter cancellation and moment calculation, Proc. ERAD, 2004, 421-424.
- 972 Stevens, B., Lenschow, D. H., Vali, G., Gerber, H., Bandy, A., Blomquist, B., Brenguier, J.-L.,
 973 Bretherton, C., Burnet, F., and Campos, T.: Dynamics and chemistry of marine
 974 stratocumulus—DYCOMS-II, *Bulletin of the American Meteorological Society*, 84, 579-
 975 594, 2003.
- 976 Stevens, B., Vali, G., Comstock, K. K., Wood, R., Van Zanten, M. C., Austin, P. H., Bretherton,
 977 C. S., and Lenschow, D. H.: Pockets of open cells and drizzle in marine stratocumulus,
 978 *Bulletin of the American Meteorological Society*, 86, 51-58, 2005.
- 979 Stevens, B., Farrell, D., Hirsch, L., Jansen, F., Nuijens, L., Serikov, I., Brüggemann, B., Forde, M.,
 980 Linne, H., and Lonitz, K.: The Barbados Cloud Observatory: Anchoring investigations of
 981 clouds and circulation on the edge of the ITCZ, *Bulletin of the American Meteorological
 982 Society*, 97, 787-801, 2016.
- 983 Tatarevic, A., Kollias, P., Oue, M., & Wang, D.: User's Guide CR-SIM SOFTWARE v
 984 3.0. McGill University Clouds Research Group, Document available at
 985 <http://radarscience.weebly.com/radar-simulators.html>. Last accessed 07/2019
 986
- 987 Torres, S. M., and Zmic, D. S.: Ground clutter canceling with a regression filter, *Journal of
 988 Atmospheric and Oceanic Technology*, 16, 1364-1372, 1999.
- 989 Toyoshima, K., Masunaga, H., and Furuzawa, F. A.: Early evaluation of Ku-and Ka-band
 990 sensitivities for the global precipitation measurement (GPM) dual-frequency precipitation
 991 radar (DPR), *Sola*, 11, 14-17, 2015.
- 992 Unal, C.: Spectral polarimetric radar clutter suppression to enhance atmospheric echoes, *Journal
 993 of atmospheric and oceanic technology*, 26, 1781-1797, 2009.

- 994 Vali, G., Kelly, R. D., French, J., Haimov, S., Leon, D., McIntosh, R. E., and Pazmany, A.:
 995 Finescale structure and microphysics of coastal stratus, *Journal of the Atmospheric*
 996 *Sciences*, 55, 3540-3564, 1998.
- 997 VanZanten, M., Stevens, B., Vali, G., and Lenschow, D.: Observations of drizzle in nocturnal
 998 marine stratocumulus, *Journal of the Atmospheric Sciences*, 62, 88-106, 2005.
- 999 Villarini, G., and Krajewski, W. F.: Review of the different sources of uncertainty in single
 1000 polarization radar-based estimates of rainfall, *Surveys in Geophysics*, 31, 107-129, 2010.
- 1001 Wang, H., and Feingold, G.: Modeling mesoscale cellular structures and drizzle in marine
 1002 stratocumulus. Part I: Impact of drizzle on the formation and evolution of open cells,
 1003 *Journal of the Atmospheric Sciences*, 66, 3237-3256, 2009.
- 1004 Warren, R. A., Protat, A., Siems, S. T., Ramsay, H. A., Louf, V., Manton, M. J., and Kane, T. A.:
 1005 Calibrating ground-based radars against TRMM and GPM, *Journal of Atmospheric and*
 1006 *Oceanic Technology*, 35, 323-346, 2018.
- 1007 Wood, R.: Drizzle in stratiform boundary layer clouds. Part II: Microphysical aspects, *Journal of*
 1008 *the Atmospheric Sciences*, 62, 3034-3050, 2005.
- 1009 Wood, R., and Hartmann, D. L.: Spatial variability of liquid water path in marine low cloud: The
 1010 importance of mesoscale cellular convection, *Journal of Climate*, 19, 1748-1764, 2006.
- 1011 Wood, R., Bretherton, C., Leon, D., Clarke, A., Zuidema, P., Allen, G., and Coe, H.: An aircraft
 1012 case study of the spatial transition from closed to open mesoscale cellular convection over
 1013 the Southeast Pacific, *Atmospheric Chemistry and Physics*, 11, 2341, 2011.
- 1014 Wood, R.: Stratocumulus clouds, *Monthly Weather Review*, 140, 2373-2423, 2012.
- 1015 Yamaguchi, T., and Feingold, G.: On the relationship between open cellular convective cloud
 1016 patterns and the spatial distribution of precipitation, *Atmospheric Chemistry and Physics*,
 1017 15, 1237, 2015.
- 1018 Yang, F., Luke, E. P., Kollias, P., Kostinski, A. B., and Vogelmann, A. M.: Scaling of drizzle virga
 1019 depth with cloud thickness for marine stratocumulus clouds, *Geophysical Research Letters*,
 1020 45, 3746-3753, 2018.
- 1021 Yuter, S. E., Serra, Y. L., and Houze Jr, R. A.: The 1997 Pan American climate studies tropical
 1022 eastern Pacific process study. Part II: Stratocumulus region, *Bulletin of the American*
 1023 *Meteorological Society*, 81, 483-490, 2000.
- 1024 Zhou, X., Heus, T., and Kollias, P.: Influences of drizzle on stratocumulus cloudiness and
 1025 organization, *Journal of Geophysical Research: Atmospheres*, 122, 6989-7003, 2017.
- 1026 Zhou, X., Ackerman, A. S., Fridlind, A. M., and Kollias, P.: Simulation of Mesoscale Cellular
 1027 Convection in Marine Stratocumulus. Part I: Drizzling Conditions, *Journal of the*
 1028 *Atmospheric Sciences*, 75, 257-274, 2018.

1029
1030
1031
1032
1033

Tables

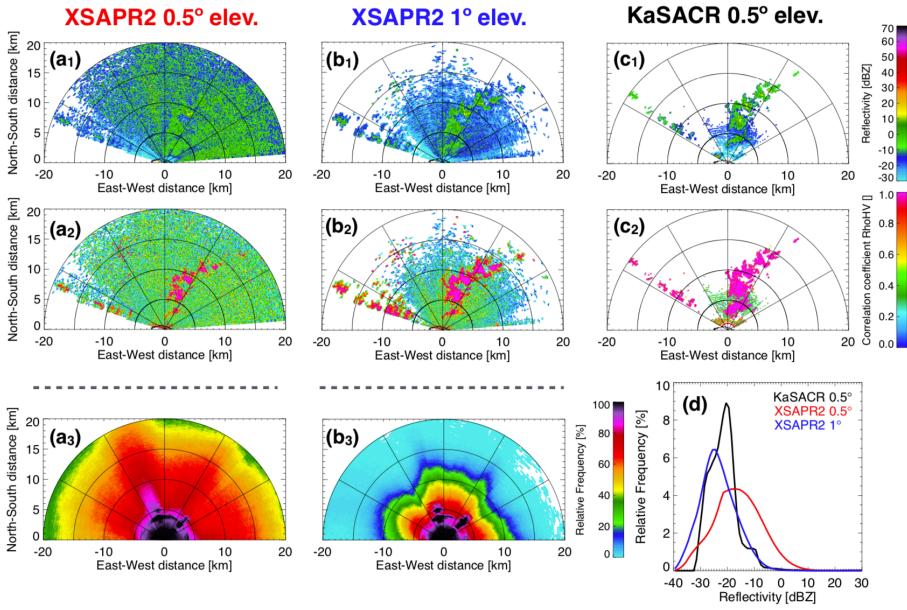
Table 1 Specification of ARM ENA zenith and scanning second generation radars

	KAZR2	KaSACR2	XSAPR2	
Frequency (MHz)	34860	35290	9500	
Peak power (kW)	2.2	2.2	300	
Maximum Duty cycle (%)	5.0	5.0	0.1	
Pulse compression	Yes	Yes (but not on)	No	
Pulse length	4 μ s	200 ns	?	0.66 μ s
Sensitivity single pulse (dBZ)	-32.5 (at 1 km)	-44 (at 1 km)	-15 (at 20 km)	-21 (at 20 km)
Dead zone (m)	72	737	400	100
Unambiguous range (km)	18	40	Over 100	
Gate spacing (m)	30	30	100	
Antenna size (m)	1.82	1.82	5.0	
3-dB Beam width (°)	0.3	0.3	0.45	
Scan rate (° s ⁻¹)	-	3	6	
Scan strategy	Zenith	PPI scan	VCP scan	
Elevation angle (°)	90	0.5	0 to 5 every 0.5	
Azimuthal sector (°)	-	360	160	
Scan time	3 s	2 min	5 min	
Scan Interval	Continuous	15 min		
Transmit polarization	H	Alternating H and V	Simultaneous H and V	
Received polarization	H and V	H and V	H and V	
Amplifier Type	Klystron (EIKA)	Klystron (EIKA)	Magnetron	
Signal processing	FFT	Pulse-pair	FFT	Pulse- pair
Doppler spectra	Yes	No	Yes	No
Second trip echo removal technique	Challenging	Frequency Hopping	Challenging	None Coherent Power technique
Velocity dealiasing technique	Challenging	Staggered Pulse Repetition Time	Challenging	Challenging

1034
1035
1036

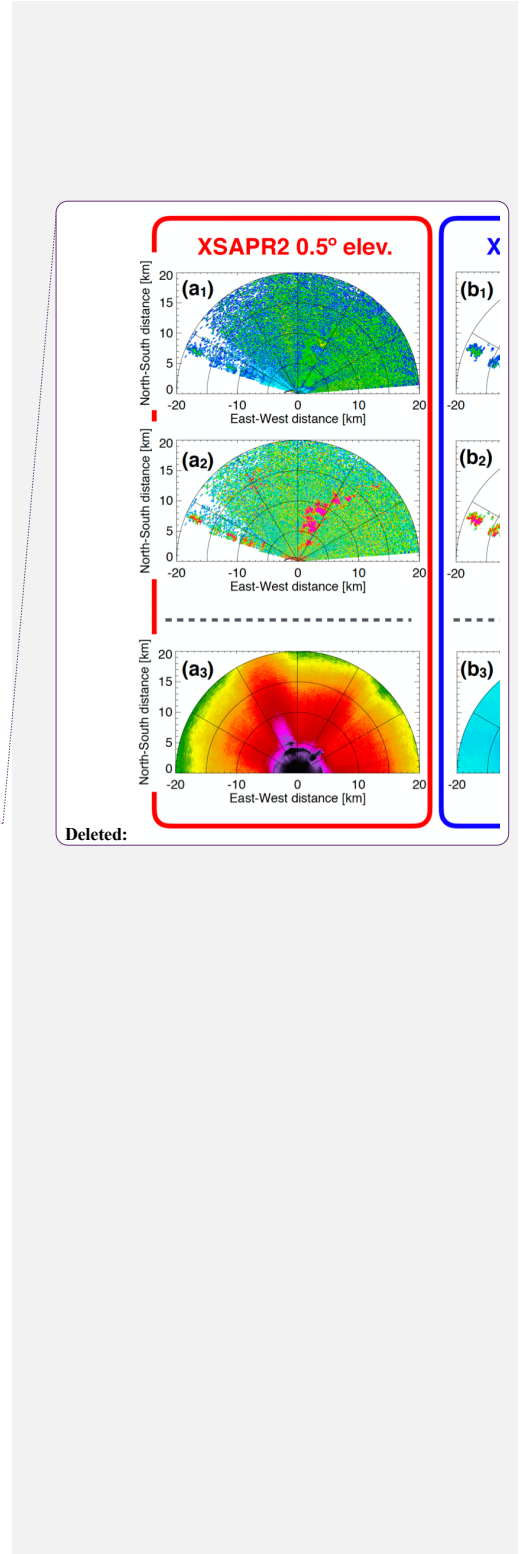
1037
1038

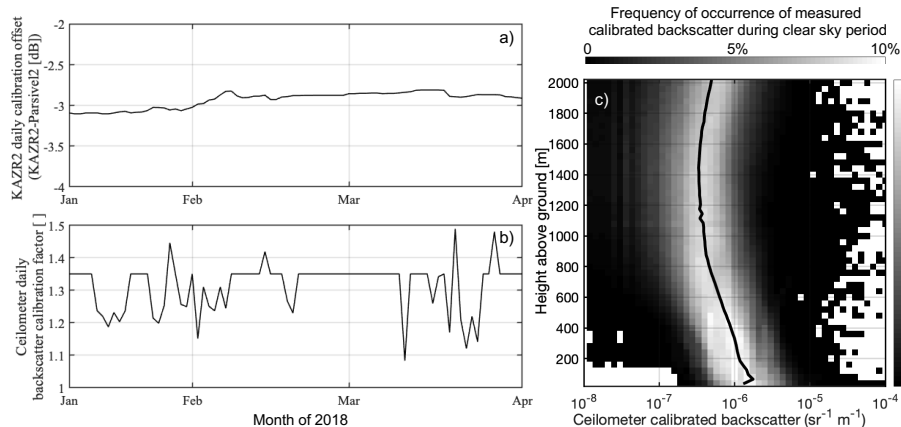
Figures



1039
1040
1041
1042
1043
1044
1045
1046

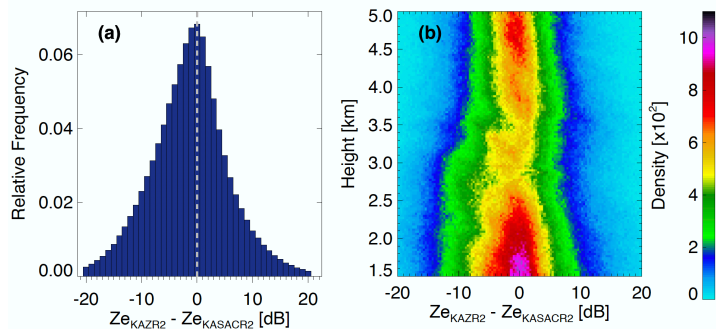
Figure 1. For significant echoes, 1) radar reflectivity, 2) correlation coefficient (ρ_{HV}) and 3) relative frequency of occurrence of clutter as observed by the a) XSAPR2 at 0.5° elevation, b) XSAPR2 at 1° elevation and c) KaSACR at 0.5° elevation. d) Clutter characteristics estimated using 93 hours of clear sky observations.





1048
1049
1050
1051
1052
1053
1054
1055
1056

Figure 2. a) Ka-band Zenith Radar (KAZR) calibration offset to be removed from the KAZR radar reflectivity in order to match Parsivel Disdrometer radar reflectivity estimates. b) Ceilometer lidar calibration factor to be multiplied to observed backscatter to match theoretical liquid cloud lidar ratios. c) Frequency of occurrence of measured backscatter during clear sky conditions, solid black line is interpreted as the mean aerosol backscatter signal, observations small than this threshold at each height are eliminated from the drizzle analysis.



1057
1058
1059
1060
1061

Figure 3. For period when KAZR2 and KaSACR2 are matched in time and range a) Difference in radar reflectivity reported by both sensors over the ranges between 1.5 and 5.0 km, b) Difference in radar reflectivity reported by both sensors as a function of range.

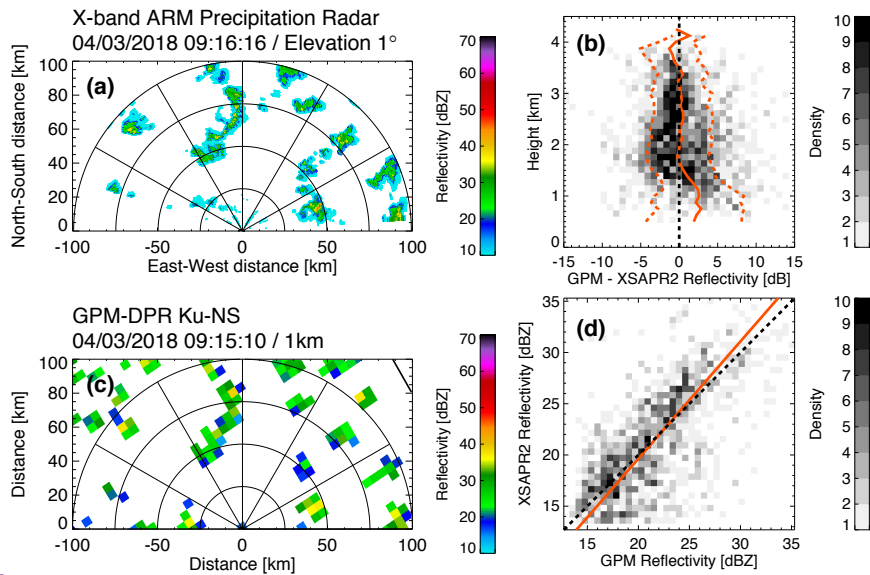
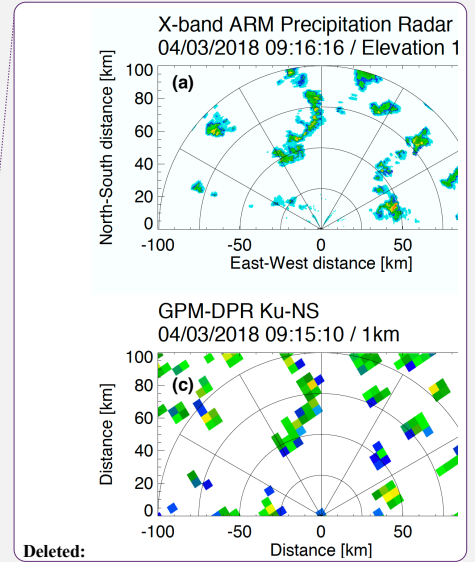
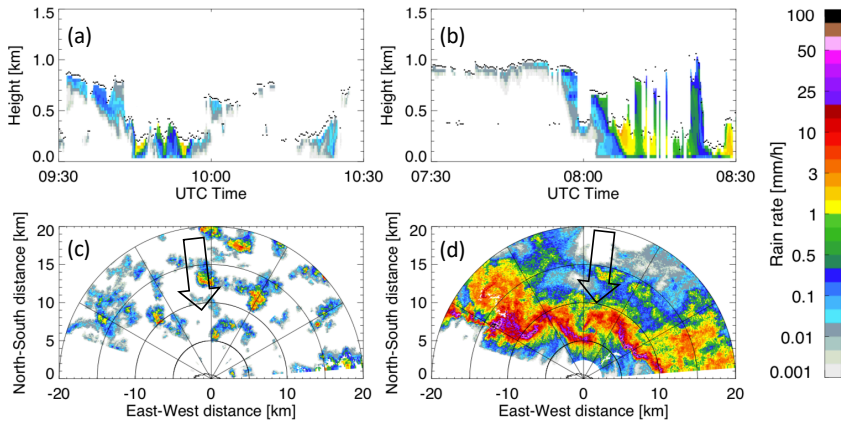


Figure 4. For the conditions that occurred on 04/03/2018 around 09:15 as observed by a) XSAPR2 radar reflectivity at 1° elevation and c) GPM-DPR Ku-band radar reflectivity at 1 km height. For the entire geometry-matching dataset with 1516 points used for the calibration b) Scatter, mean (orange) and standard deviation (dashed lines) of the difference between the GPM-DPR Ku-band and XSAPR2 radar reflectivity measurements as a function of height and d) scatterplot comparing the XSAPR2 and GPM-DPR Ku-band reflectivities measurements above the GPM surface echo height of 1.5 km; Also plotted is the 1-to-1 relationship (dashed line) and the best linear fit to the observations (solid orange line).



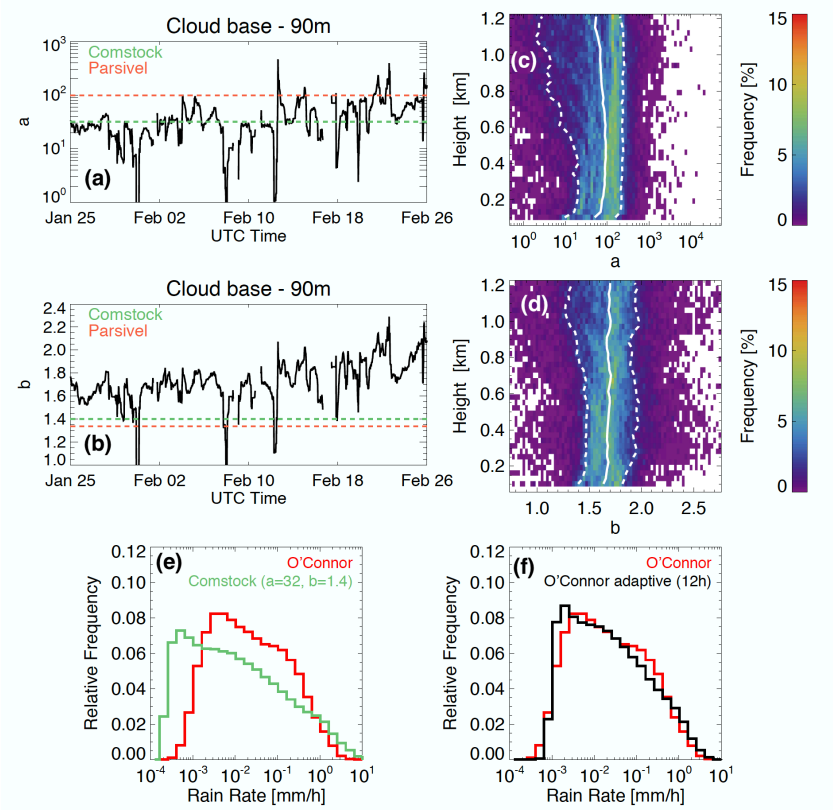
Deleted: Difference
 Deleted:
 Deleted: .

1062
 1063
 1064
 1065
 1066
 1067
 1068
 1069
 1070
 1071
 1072
 1073
 1074



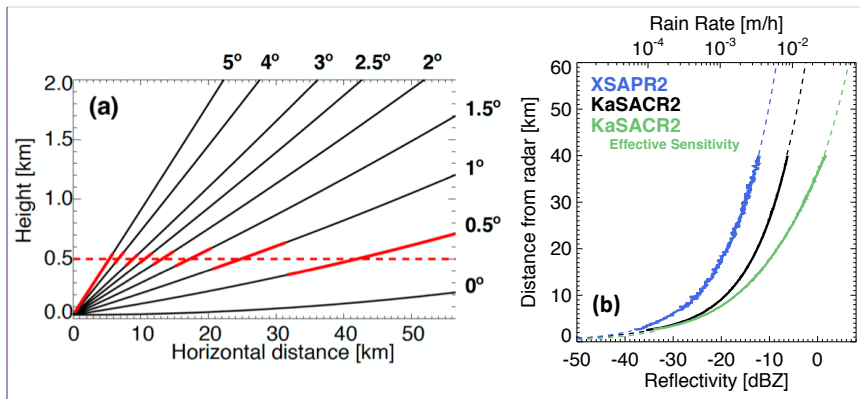
1079
 1080 **Figure 5.** Retrieval of popcorn convection precipitation rate on 02/02/2018 using a) KAZR2
 1081 (zenith between 9:30 to 10:30 UTC) and c) KaSACR2 (1° elevation PPI at 10:00 UTC). Retrieval
 1082 of squall line precipitation rate on 02/03/2018 using b) KAZR2 (zenith between 7:30 to 8:30 UTC)
 1083 and d) KaSACR2 (1° elevation PPI at 8:00 UTC). Also indicated are the location of cloud bases
 1084 (black dots in panels a-b) and the general wind direction (arrows in panels c-d). Note that KAZR2
 1085 is located at (0 km,0 km).
 1086

Deleted: <object>
 Deleted: 3
 Deleted: 2
 Deleted: .



1091 **Figure 6.** Time series of the α (a) and β (b) coefficients used to estimate precipitation rate 90
 1092 m below cloud base height for a 30-day long period that overlaps with the second phase of the
 1093 ACE-ENA field campaign. For the same time period, distribution of the α (c) and β (d)
 1094 coefficients with height along with their median (solid line) and 25th and 75th percentile values
 1095 (dashed line). Precipitation rate distributions retrieved using the O'Connor et al. (2005)
 1096 technique (red) and estimated using the adaptive coefficients (f, black) or the fixed coefficients
 1097 proposed by Comstock et al., [2004] (e, green). Comstock et al., [2004] coefficients and
 1098 coefficients determined from disdrometer observations are both presented in panels a and b
 1099 using dashed green lines and orange lines respectively.
 1100
 1101

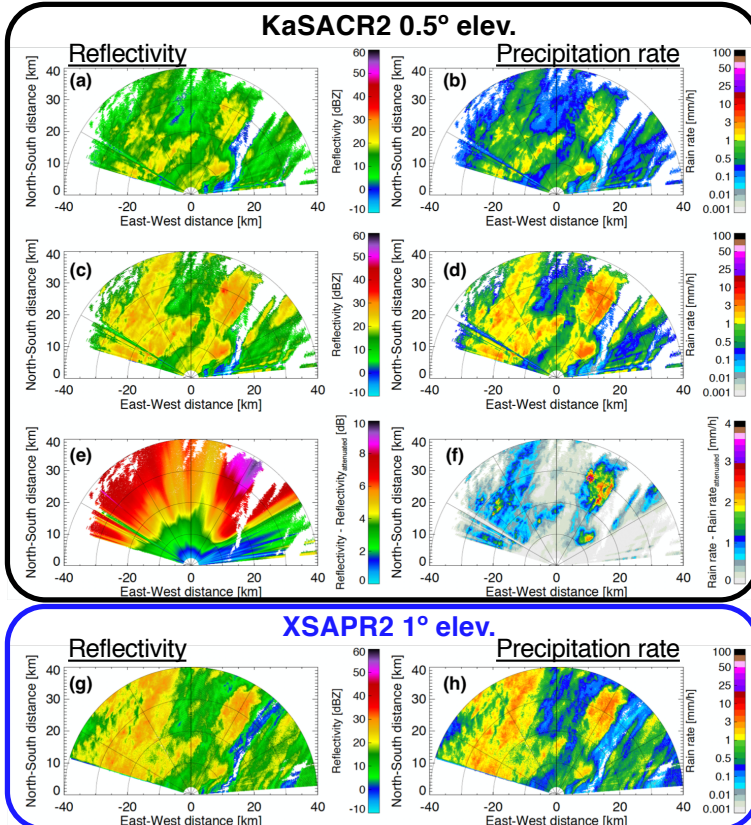
Deleted: 6



Commented [LK2]: Old Figure 9 without the CAPPI

1103
 1104
 1105
 1106
 1107
 1108
 1109
 1110
 1111

Figure 7. a) PPI scan geometry and b) Theoretical sensitivity of the XSAPR2 (blue) and KaSACR2 (black) along with the KaSACR2 “effective” sensitivity considering it is affected by gas attenuation (green).



1112
 1113 **Figure 8.** Example of observations/retrievals of the conditions happening on 02/13/2018 at
 1114 00:10 UTC. Shown for KaSACR2 performing 0.5° elevation PPI a) radar reflectivity field
 1115 corrected for gaseous attenuation neglecting liquid water attenuation and b) corresponding
 1116 precipitation rate retrieved using adaptive Z-R relationships; c) radar reflectivity field
 1117 corrected for both gas and liquid water attenuation and d) corresponding precipitation rate; e)
 1118 difference between a and c showing the range-accumulated radar reflectivity liquid water
 1119 attenuation correction and f) the corresponding precipitation rates bias. The bottom panels (g)
 1120 and (h) show simultaneously collected XSAPR2 1.0° PPI observations for reference.

Deleted: 7

Deleted: upper

Deleted: f

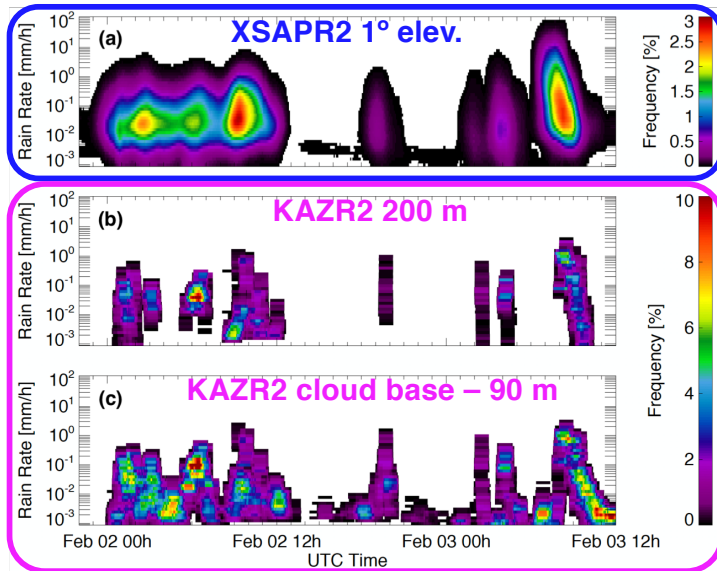
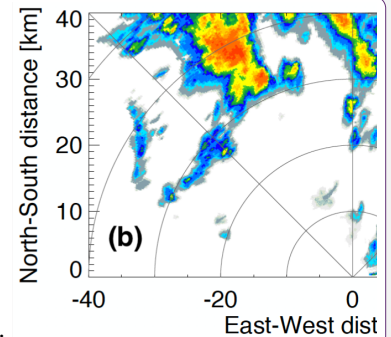


Figure 9. For a 36-h period (00:00 UTC February 2 to 12:00 UTC February 3), hourly probability density functions (pdfs) of precipitation rate estimated from a) XSAPR2 when performing a 1° elevation PPI scan, b) KAZR2 200 m from the surface and c) KAZR2 90 m below cloud base height

1126
 1127
 1128
 1129
 1130
 1131
 1132
 1133
 1134
 1135
 1136
 1137
 1138

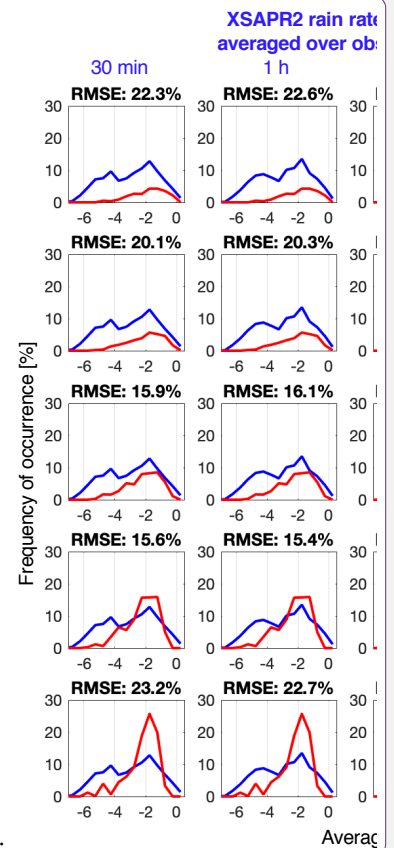
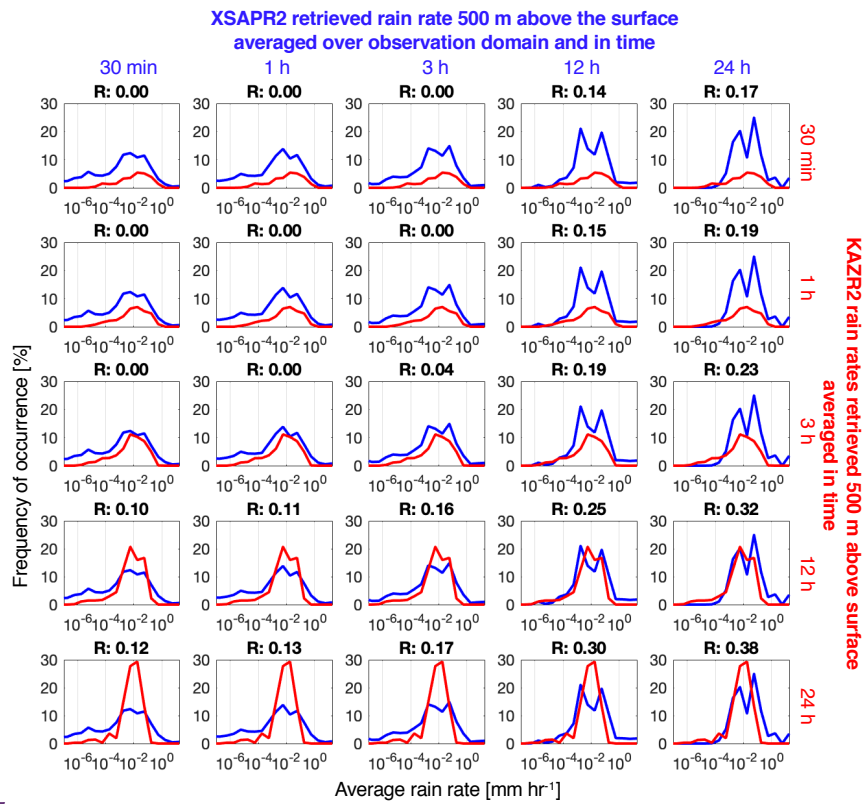
Deleted: 8



Deleted:

Deleted: ¶

Figure 9. a) PPI scan geometry and b) Cartesian coordinate constant altitude plan position indicator (CAPPI) map of precipitation rate constructed around an altitude of 500 m using XSAPR2 observations collected 21/02/2018 on at 15:00 between 1 and 5° elevation. c) Theoretical sensitivity of the XSAPR2 (blue) and KaSACR2 (black) along with the KaSACR2 “effective” sensitivity considering it is affected by gas attenuation (green). ¶



- Deleted:
- Deleted: 0
- Deleted: at 1° elevation over the domain between 2.5 and 40 km (blue) and as estimated
- Deleted: at 200 m
- Deleted:)
- Deleted: .
- Deleted: root mean square error
- Deleted: MSE
- Deleted: on the frequency of occurrence of precipitation rate estimated in 0.5 mm hr^{-1} bins between 10^{-8} and 10^0 mm hr^{-1} .

1150
1151
1152
1153
1154
1155
1156
1157
1158

Figure 10. Probability density function of average (over different time windows) precipitation rate as estimated the XSAPR2 and by the KAZR2 (red) both at 500 m above the surface in $10^{0.5} \text{ mm hr}^{-1}$ bins; The XSAPR2 precipitation rates 500 m above the surface being from gridded CAPPI constructed using a collection of PPI scans and are limited to the domain between 2.5 and 40 km around the location of the KAZR2. Over each box is the correlation coefficient (R) between the XSAPR2 and the KAZR2 average precipitation rates.